

1 **Glacial and environmental changes in northern Svalbard over the last 16.3**
2 **ka inferred from neodymium isotopes**

3
4 Kwangchul Jang^a, Youngkyu Ahn^a, Young Jin Joe^a, Carmen A. Braun^b, Young Ji Joo^{a,1}, Jung-Hyun
5 Kim^a, Germain Bayon^c, Matthias Forwick^b, Christoph Vogt^d, Seung-Il Nam^a

6
7
8 ^aKorea Polar Research Institute, Incheon 21990, Republic of Korea

9 ^bUiT The Arctic University of Norway, Department of Geosciences, NO-9037 Tromsø, Norway

10 ^cIFREMER, Marine Geosciences Unit F-29280 Plouzané, France

11 ^dCrystallography, FB05 Geosciences & MARUM, University of Bremen, Klagenfurter Strasse 2-4,
12 28359 Bremen, Germany

13
14
15
16
17 Submitted to *Global and Planetary Change*, October 2020

18 1st Revision submitted March 2020

19
20
21 *Corresponding author. Tel.: +82-32-760-5362; Fax: +82-32-760-5397; E-mail: sinam@kopri.re.kr

22 ¹Present address: Department of Earth and Environmental Sciences, Pukyong National University,
23 Busan 48513, Republic of Korea

24

25 **Abstract**

26 The reconstruction of past ice sheet extents and dynamics in polar regions is essential for
27 understanding the global climate system and obtaining more reliable predictions of future climate
28 change. Here, we present a multi-proxy dataset integrating the Nd isotopic compositions (ϵ_{Nd}) of
29 paired detrital and authigenic iron oxide fractions, grain size distributions, organic geochemistry, and
30 mineral assemblages in a glaci-marine sediment core (core HH17-1085-GC) retrieved from the
31 continental shelf off northern Svalbard. Our results indicate variability in sediment provenance and
32 chemical weathering patterns since the last deglaciation, allowing us to distinguish a succession of
33 distinct paleoclimate events: 1) a general retreat of the Svalbard-Barents Sea Ice Sheet (SBIS) from
34 the continental shelf before ca. 16.3 ka BP; 2) an intense episode of meltwater discharge related to
35 massive glacier loss between ca. 12.1 – 9.9 ka BP; and 3) a period of reduced meltwater input
36 between ca. 9.9 and ca. 2.7 ka BP followed by 4) a phase of glacier re-advance over the last two
37 millennia. Evidence for the prolonged supply of radiogenic detrital ϵ_{Nd} and dolomite at the site of core
38 HH17-1085-GC indicates that the onset of deglaciation offshore northeastern Svalbard may have
39 occurred at least 1 ka later than that at the northwestern shelf, which can be further evaluated by
40 obtaining a more precise end-member determination for the northeastern source with a quantitative
41 ϵ_{Nd} dataset from Nordaustlandet. In the context where both polar sea-ice and oceanic circulation are
42 expected to have played minor roles in determining the ϵ_{Nd} composition of sedimentary Fe
43 oxyhydroxide phases, the evidence for pronounced Nd isotopic decoupling between paired authigenic
44 and detrital signatures ($\Delta\epsilon_{Nd}$) at ca. 15.2 and 14.1 ka BP is interpreted as reflecting chemical
45 weathering changes following the retreat of the SBIS on northern Svalbard, probably corresponding to
46 punctual episodes of glacial re-advances. Our findings provide a better understanding of the deglacial
47 history of northern Svalbard during and after the last deglaciation and highlight the utility of Nd
48 isotopes as a proxy for reconstructing paleo-cryosphere changes.

49

50 **Keywords:** Neodymium isotopes, Svalbard-Barents Sea Ice Sheet, Hinlopen Strait, Svalbard, glacial
51 activity

52 1. Introduction

53 The Arctic Ocean has repeatedly undergone dramatic changes in the extent of ice coverage
 54 over glacial-interglacial cycles (review in Darby et al., 2006; Jakobsson et al., 2014; Stein, 2019).
 55 Since any change in the ice budget of polar regions exerts a strong influence on the global climate
 56 system through its impacts on ice albedo, freshwater removal/input to the ocean, and ocean circulation
 57 (e.g., Curry et al., 1995; Jang et al., 2013; Tarasov and Peltier, 2005), reconstructing the history of ice
 58 coverage within and around the Arctic Ocean can provide critical insights into our understanding of
 59 past, present, and future climate change. Svalbard is a key location for investigating past climate
 60 changes in the Arctic because this archipelago has been affected by various ice types during multiple
 61 glacial-interglacial cycles, including ice sheets, glaciers, and sea-ice. The general contour and extent
 62 of the Svalbard-Barents Sea Ice Sheet (SBIS) and glaciers on Svalbard during and after the Late
 63 Weichselian have been discussed for several decades (for the glaciers from Fjeldskaar et al., 2018 and
 64 references therein; for the ice sheet from Hughes et al., 2016 and references therein). However, most
 65 of these earlier studies focused predominantly on western Svalbard (e.g., Ebbesen et al., 2007;
 66 Elverhøi et al., 1995; Svendsen et al., 1996).

67 Previous inferences of the glacial activity on the continental shelf off northern Svalbard have
 68 been based primarily on the occurrence of ice-rafted debris (IRD) and microfossils (e.g., core NP94-
 69 51 from Jernas et al., 2013; Koç et al., 2002; Ślubowska et al., 2005). Additionally, the ratio of
 70 neodymium (Nd) isotopes ($^{143}\text{Nd}/^{144}\text{Nd}$), expressed using the epsilon notation $\epsilon_{\text{Nd}} =$
 71 $[(^{143}\text{Nd}/^{144}\text{Nd})_{\text{sample}} / (^{143}\text{Nd}/^{144}\text{Nd})_{\text{CHUR}} - 1] \times 10^4$, where $(^{143}\text{Nd}/^{144}\text{Nd})_{\text{CHUR}}$ is 0.512638 (Jacobsen and
 72 Wasserburg, 1980), is a powerful proxy in paleoclimate studies (Goldstein and Hemming, 2003; Jang
 73 et al., 2020). However, this tracer has yet to be applied for the reconstruction of past glacial activity
 74 offshore northern Svalbard. The ϵ_{Nd} signatures of the detrital fractions of marine sediments are
 75 inherited from their source rocks on continents, and hence their variation in sedimentary records can
 76 be used to track past changes in sediment provenance (e.g., Grousset et al., 1988; Horikawa et al.,
 77 2015; Jang et al., 2017; Revel et al., 1996). In glacial marine environments around Svalbard, sediment
 78 delivery is primarily related to the advance and retreat of ice sheets and/or glaciers in nearby drainage

79 systems such that inferred provenance changes based on detrital ϵ_{Nd} can offer key information on the
80 history of ice coverage patterns (e.g., Horikawa et al., 2015; Pereira et al., 2020). Recently, Jang et al.
81 (2020) showed that the ϵ_{Nd} difference between the detrital and leached iron oxide fractions from fjord
82 sediments ($\Delta\epsilon_{Nd}$) could also provide information on past glacier fluctuations. This new approach is
83 based on the evidence that intense incongruent weathering of freshly exposed silicate rock substrates
84 occurs during periods of glacier advance, resulting in enhanced Nd isotopic decoupling (i.e. higher
85 $\Delta\epsilon_{Nd}$ differences) (Jang et al., 2020). The use of Nd isotopes in both detrital and leached iron oxide
86 fractions of fjord sediments can thus provide useful information about the extent of ice sheets and
87 glaciers in Arctic regions.

88 This paper presents Nd isotope ratios measured from the detrital and authigenic iron oxide
89 fractions of glacial marine sediments retrieved from the continental shelf off northern Svalbard to
90 reconstruct the glacial history of the northern parts of the archipelago over the last 16.3 ka.
91 Furthermore, detrital ϵ_{Nd} records are supplemented and integrated with information about sediment
92 structure, grain size, mineral assemblage, and organic geochemistry to reconstruct past changes in
93 sediment provenance. Additionally, the ϵ_{Nd} difference between paired authigenic Fe oxide and detrital
94 fractions ($\Delta\epsilon_{Nd}$) is used as a proxy for glacial weathering to identify past periods of ice sheet
95 instability and/or glacier fluctuation.

96

97 **2. Physiographic setting**

98 The Svalbard archipelago is located between 74 and 81°N and 10 and 35°E (Fig. 1A). It
99 includes nine main islands, with Spitsbergen being the largest. Two different water masses bathe
100 northern Svalbard: 1) the warm Atlantic Water (AW) carried by the Svalbard branch of the West
101 Spitsbergen Current (WSC) and 2) the cold Arctic Water (ArW) carried by the East Spitsbergen
102 Current (ESC) (Fig. 1B). Glacial troughs (~400 m deep) and shallower banks (Ottesen et al., 2007)
103 characterize the continental shelf offshore northern Svalbard. This study focuses on the area offshore
104 northern Spitsbergen where the trough continuing from Wijdefjorden and Hinlopen Trough merge.

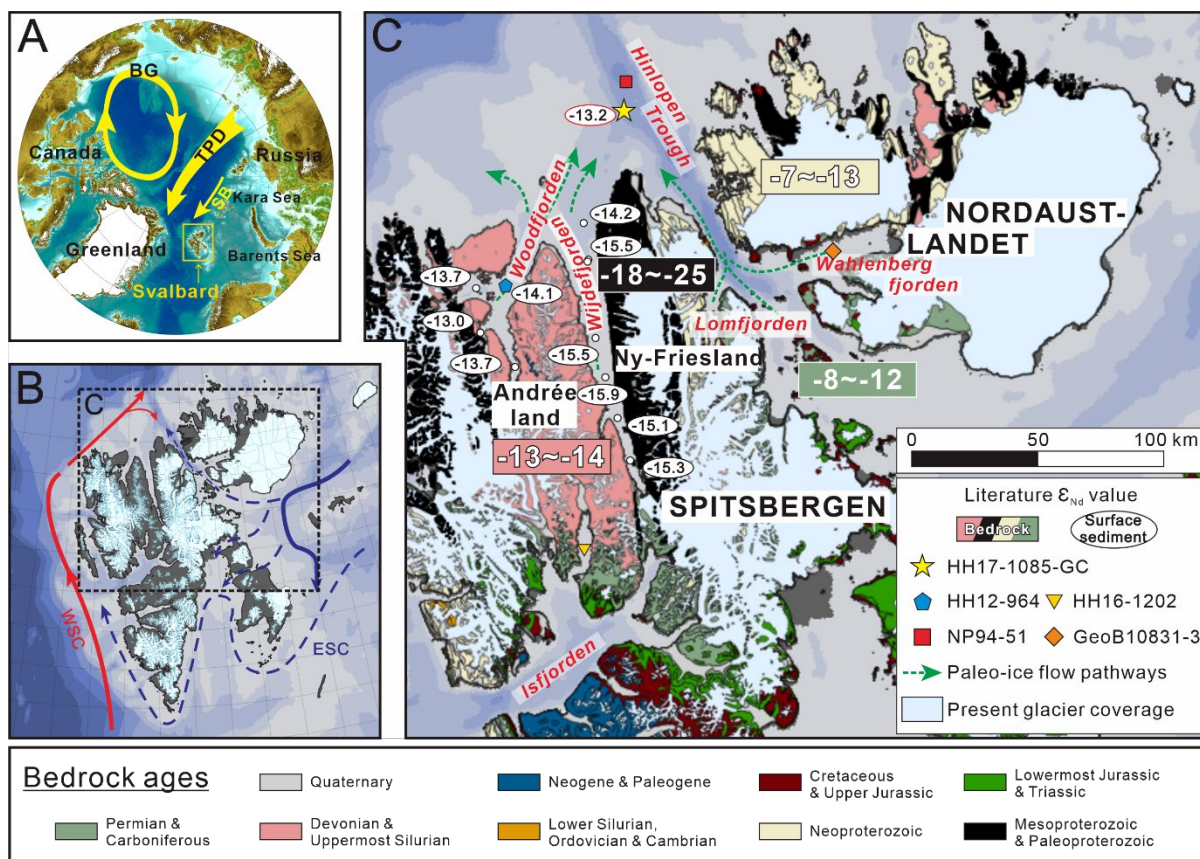


Figure 1. (A) Map of the Arctic. The location of Svalbard is marked with the yellow rectangle, and water circulation patterns including the Beaufort Gyre (BG), Transpolar Drift (TPD) and Siberian Branch (SB) are indicated by yellow arrows. (B) Map of the Svalbard archipelago and surrounding waters. The West Spitsbergen Current (WSC) and the East Spitsbergen Current (ESC) are marked with red and blue arrows, respectively. (C) Map of northern Svalbard. The sampling site of core HH17-1085-GC and comparative sites of HH12-964, HH16-1202, NP94-51 and GeoB10831-3 are indicated. The Nd isotopic compositions (ϵ_{Nd}) of detrital or bulk fractions in bedrock (rectangles) and surface sediments (ellipses) near sampling site of core HH17-1085 (yellow star) are shown (data from Jang et al., 2020; Johansson et al., 1995, 2000, 2002; Johansson and Gee, 1999). Various bedrock ages are indicated by different colors. The proposed pathways of ice streams and sediment delivery in northern Svalbard are indicated by green dashed arrows (Batchelor et al., 2011; Dowdeswell et al., 2010), and present areas of glacier coverage are colored sky blue.

105 There were several ice types on the archipelago during the Late Quaternary, including ice sheets,
 106 glaciers, and sea-ice in various configurations and extents. For example, during glacial periods this
 107 area was affected by glaciers/ice streams draining the SBIS (Ottesen et al., 2007). Sea-ice formation
 108 also occurs locally on Svalbard (Allaart et al., 2020; Bartels et al., 2017; Berben et al., 2017), and it
 109 can be transported to the area from the Arctic shelves via the Siberian Branch of the Transpolar Drift
 110 (TPD) (Tütken et al., 2002; Werner et al., 2014) (Fig. 1A). The Hinlopen Trough currently represents
 111 the main passage for the two main water masses in the area: 1) the southward inflow of the WSC and

112 2) the northward outflow of the ESC (Menze et al., 2019). However, during the Late Weichselian, it
113 also acted as a major pathway for ice flow and sediment delivery (Batchelor et al., 2011) (Fig. 1C).

114 Based on the geological setting and regional ocean circulation patterns, the main source areas
115 of terrigenous sediments deposited at the core site include Wijdefjorden and Woodfjorden on
116 Spitsbergen and Nordaustlandet. Wijdefjorden is the longest fjord system on Svalbard. It separates
117 Andrée Land to the west, where the outcrops comprise sedimentary rocks, including Devonian Old
118 Red Sandstones, and Ny-Friesland to the east, where the outcrops comprise mainly Proterozoic
119 metamorphic basement rocks (Dallmann, 2015; Hjelle, 1993) (Fig. 1C). In Woodfjorden, the bedrock
120 geology is dominated by the Devonian Old Red Sandstone, with a minor contribution of Quaternary
121 volcanic and Proterozoic rocks (Dallmann, 2015; Hjelle, 1993). In Nordaustlandet, Neoproterozoic
122 and Permian to Carboniferous rocks are the main source rocks (Fig. 1C). The sediments deposited at
123 the Arctic shelves can be further redistributed by sea-ice drifting as observed in the Fram Strait
124 (Maccali et al., 2013; Tütken et al., 2002; Werner et al., 2014). Potential source regions include all
125 areas surrounding the Arctic Ocean (i.e., the western and eastern Arctic) (Maccali et al., 2013).
126 However, in the eastern Fram Strait, sediment sources are mostly restricted to the Eurasian shelf
127 sediments (Tütken et al., 2002; Werner et al., 2014), in particular, the Kara Sea shelf (Pfirman et al.,
128 1997; Werner et al., 2014), which presumably reflect the Siberian Branch-dominated water circulation
129 pattern in the east. Given the position of our core site, located further eastward of eastern Fram Strait
130 (Fig. 1), we consider exclusively the Kara Sea shelf sediments as a potential end-member of sea-ice-
131 derived sediments from within the Arctic Ocean.

132

133 **3. Glacial history**

134 According to the time-slice reconstruction of past Eurasian ice sheets (Hughes et al., 2016;
135 Patton et al., 2017; Patton et al., 2016; Svendsen et al., 2004), Svalbard, apart from some nunataks
136 (e.g., Landvik et al., 1998) was entirely covered by the SBIS extending to the continental shelf edges
137 north and west of the archipelago during the Late Weichselian. The deglaciation from the shelf edges
138 started ca. 19 ka BP (Jessen et al., 2010). A period of comparatively slow retreat between 17-16 ka BP

139 was followed by a more rapid ice sheet retreat towards the western and northern coasts of Svalbard at
140 ca. 15 ka BP (Elverhøi et al., 1995; Landvik et al., 1998; Svendsen et al., 1992). The ice front reached
141 the mouth of Wijdefjorden before ca. 14.5 ka BP (Allaart et al., 2020). The outer fjords of Svalbard
142 were mostly ice-free after ca. 12 ka BP (Farnsworth et al., 2020; Hughes et al., 2016). In the inner
143 fjords, the timing of the deglaciation varied depending on the location. For example, the deglaciation
144 terminated in Isfjorden at approximately 11.2 ka BP (Baeten et al., 2010; Elverhøi et al., 1995;
145 Forwick and Vorren, 2009) and in Wijdefjorden at approximately 7.2 ka BP (Allaart et al., 2020;
146 Braun, 2019).

147 The glacial coverage on Svalbard at ca. 10 ka BP remains controversial, with some models
148 suggesting fully deglaciated conditions (e.g., the minimum and most-credible glacial scenario of
149 Hughes et al., 2016) and others suggesting present-day glacier limits (e.g., the maximum glacial
150 scenario of Hughes et al., 2016). While a recent modeling study supports the latter scenario based on
151 sea-level observations (Fjeldskaar et al., 2018), a recently published data compilation suggests an
152 intermediate glacial coverage between the aforementioned scenarios (Farnsworth et al., 2020).

153 During the early Holocene, the glacial coverage decreased, reaching a minimum extent at the
154 beginning of the middle Holocene (ca. 8.0-6.0 ka BP; Farnsworth et al., 2020; Fjeldskaar et al., 2018).
155 Massive glaciers on Svalbard, such as the ice caps on Nordaustlandet and in eastern Spitsbergen,
156 survived the Holocene Thermal Optimum (ca. 11.2-5.2 ka BP; Fjeldskaar et al., 2018), whereas
157 smaller glaciers had mostly vanished by ca. 7.5-5.5 ka BP (Fjeldskaar et al., 2018). Subsequently, the
158 glaciers began to grow or reform, as recorded in glacial-marine and lake sediments (Baeten et al., 2010;
159 Forwick et al., 2010; Røthe et al., 2015; Svendsen and Mangerud, 1997; van der Bilt et al., 2015), and
160 reached their maximum post-glacial extents at various times during the late Holocene (Dowdeswell et
161 al., 2020; Kempf et al., 2013; Martín-Moreno et al., 2017).

162

163 **4. Materials and methods**

164 *4.1. Sample collection*

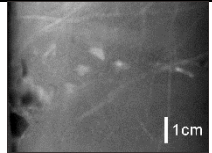
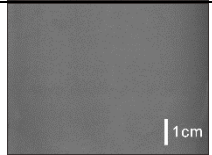
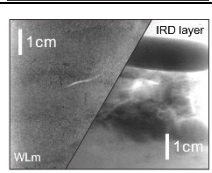
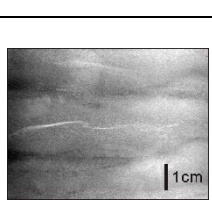
165 Sediment gravity core HH17-1085-GC (hereafter referred to as 1085-GC) (80.274°N,

166 16.211°E, ~322 m water depth; 462 cm long) provides the basis for this study. It was retrieved from
 167 the continental shelf off northern Spitsbergen during the 2nd Korea-Norway joint cruise of *RV Helmer*
 168 *Hanssen* (UiT The Arctic University of Norway) in 2017 (Fig. 1). The core site is located at the
 169 merger of a trough continuing as an extension of Wijdefjorden and the Hinlopen Trough. The
 170 temperature (T ~1.6 °C) and salinity (S ~34.77 psu) of the bottom water at the site of 1085-GC differ
 171 slightly from those of the AW, characterized by T > 3.0 °C and S > 34.65 psu (Cottier et al., 2005),
 172 probably due to the mixing of the AW with the ArW transported by the ESC (-1.5 < T < -1.0 and 34.30
 173 < S < 34.80) (Cottier et al., 2005).

174 Braun (2019) performed laboratory work at UiT to determine the physical properties of the
 175 core and to acquire line-scan images and x-radiographs of the core (Table 1 and Fig. 2). Briefly, the
 176 wet bulk density and magnetic susceptibility of the whole core were determined at 1 cm intervals
 177 using a GEOTEK Multi-Sensor Core Logger (MSCL). The x-radiographs and line-scan images of the
 178 split cores were acquired using the GEOTEK MSCL-XCT X-ray imaging machine and the Avaatech
 179 XRF core scanner, respectively. The darker intervals on the x-radiographs indicate denser materials.

180

181 **Table 1.** Summary of sedimentary facies in core HH17-1085-GC.

Unit	Facies / core depth	X-radiograph	Description	Depositional process
B2	Bioturbated sandy mud (Bsm) 30-0 cm		Dark grayish brown; sandy mud with some IRD (> 1 mm); poorly sorted; intensely bioturbated	Hemipelagic settling affected by drifting ice (sea-ice)
B1	Massive mud (Mm) 228-30 cm		Dark grayish brown; silt-rich massive mud, upward coarsening, IRD rare; poorly sorted; no primary structure, homogenous; a pale brown clay-rich layer at the base of this unit	Suspension plumes from meltwater plumes in ice-distal environment
A2	Weakly laminated mud (WLm) 385-228 cm		Mostly dark grayish brown; relatively silt-rich; poorly sorted; lamination blurred and more poorly defined upward in the core; an IRD-rich coarse layer between 360 and 370 cm (right part of figure)	Suspension settling from meltwater plumes in transitional environments from ice-proximal to ice-distal
A1	Laminated mud (Lm) 462-385 cm		Alteration between dark reddish gray and dark grayish brown; silt-rich and clay-rich muds without IRD; very poorly sorted; distinct and well laminated with good lateral continuity, lamination subparallel to slightly wavy	Suspension settling from meltwater plumes in ice-proximal environment.

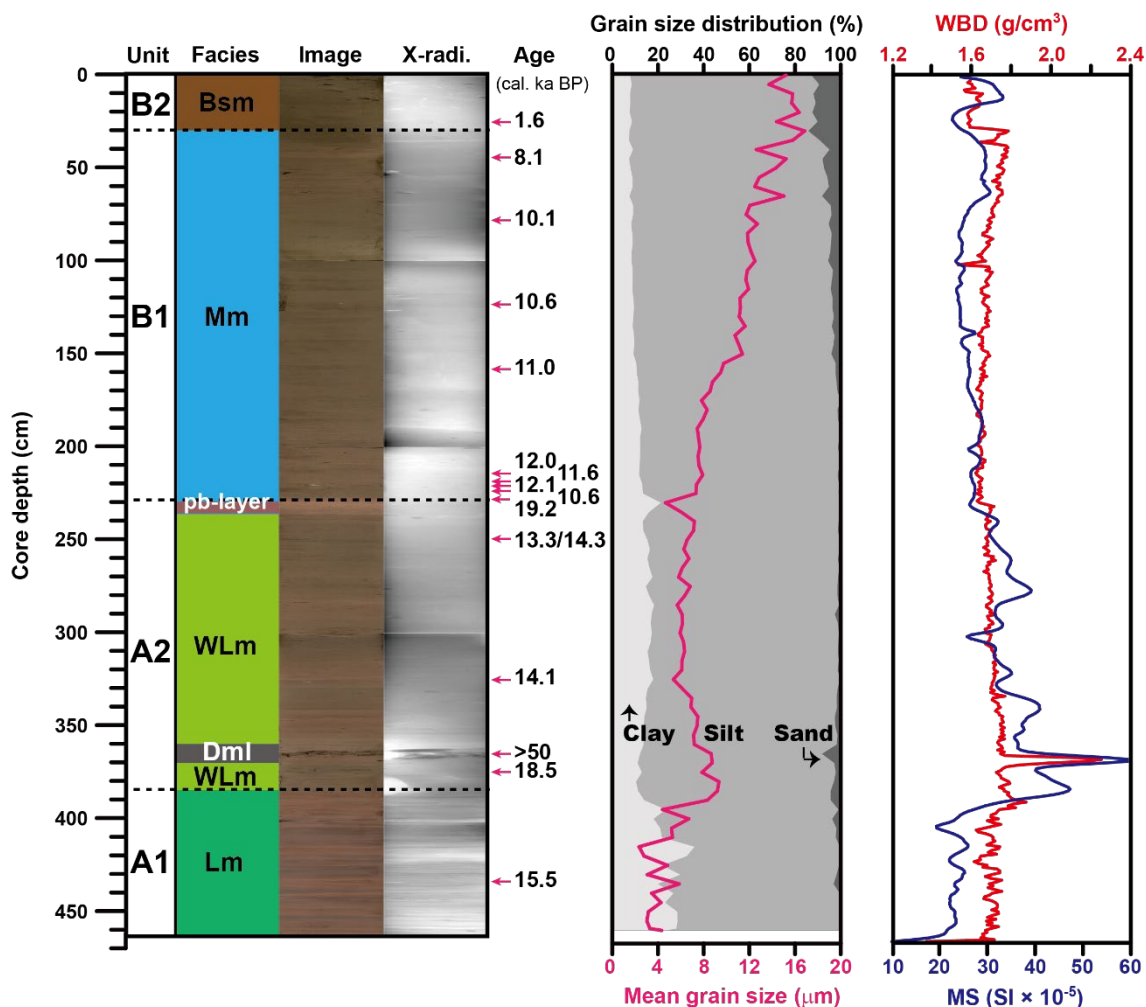


Figure 2. Lithostratigraphic units and facies of core HH17-1085-GC based on line scan images and x-radiographs and grain size distribution, mean grain size, wet bulk density (WBD) and magnetic susceptibility (MS). BSM: bioturbated sandy mud; Mm: massive mud; pb-layer: pale-brown layer; WLm: weakly laminated mud; Dml: diamicton with lamination; Lm: laminated mud. The calibrated ^{14}C ages are indicated. For details, see Table 1.

182

183 4.2. Grain size analysis

184 The grain size distributions were measured at 5 cm intervals using a laser diffraction
 185 instrument (Mastersizer 3000, Malvern) at the Korea Polar Research Institute (KOPRI). Before
 186 measurement, each sample was freeze-dried and then treated with 35 % hydrogen peroxide to remove
 187 organic matter. Coarse grains larger than 1 mm (hereafter referred to as IRD) were counted at 1 cm
 188 intervals from x-radiograph images by Braun (2019). The mean sizes were calculated with
 189 GRADISTAT v 8.0 (Blott and Pye, 2001) using the method of Folk and Ward (1957).

190

191 4.3. AMS ¹⁴C age dating

192 The age model for core 1085-GC is based on the integration of results from Braun (2019)
 193 and additional AMS ¹⁴C analyses using the MICADAS system at the Alfred Wegner Institute –
 194 Helmholtz Centre for Polar and Marine Research (Table 2 and Fig. 3). The AMS ¹⁴C ages were
 195 converted into calendar ages by applying the Marine13 dataset of the Calib Rev 7.0.4 program
 196 (Stuiver and Reimer, 1993) with $\Delta R = 105 \pm 24$ yr for all samples (Mangerud et al., 2006). After
 197 rejecting four ¹⁴C ages (Table 2; for details, see section 5.2), the age-depth model was determined with
 198 Bayesian age-depth modeling in BACON (v. 2.2; Blaauw and Christen, 2011) using R (v. 4.0.0; R
 199 Development Core Team 2020). We employed the default settings except for Student's t-distribution
 200 parameters t.a and t.b. The adjustments of those parameters (from t.a = 3 and t.b = 4 to t.a = 33 and t.b
 201 =34) allowed the most recent age control point to be included in the age-depth model with a less
 202 smoothed age-depth relationship.

203 **Table 2.** AMS ¹⁴C ages and converted calendar ages of core HH17-1085-GC

Lab ID	Unit	Core depth (cm)	AMS ¹⁴ C age (yr BP)	Cal. age (yr BP)	Material dated	References
Beta-529788	B2	25.5	2110 ± 30	1569 ± 63	Mollusk	This study
AWI 5473.1.1	B1	44.5	7694 ± 82	8053 ± 182	Mixed foram.	This study
AWI 5474.1.1	B1	79.5	9386 ± 92	10082 ± 315	Mixed foram.	This study
Beta-529789	B1	122.5	9780 ± 30	10573 ± 62	Mollusk	This study
AWI 5475.1.1	B1	159.5	10168 ± 97	11046 ± 279	Mixed foram.	This study
AWI 5476.1.1	B1	214.5	10738 ± 103 [#]	11957 ± 520	Mixed foram.	This study
Beta-546258	B1	219.5	10570 ± 30	11606 ± 132	Mollusk	This study
AWI 2740.1.1	B1	221.5	10829 ± 39 [#]	12143 ± 141	Mollusk	Braun (2019)
AWI 5103.1.1	B1	224.5	9827 ± 100	10627 ± 216	Mixed foram.	This study
AWI 5104.1.1	A2	229.5*	16492 ± 158 [#]	19282 ± 269	Mixed foram.	This study
AWI 5477.1.1	A2	249.5	11885 ± 107	13253 ± 241	Mixed foram.	This study
AWI 5478.1.1	A2	249.5**	12794 ± 155 [#]	14344 ± 484	Mollusk	This study
AWI 2742.1.1	A2	326	12696 ± 40	14076 ± 80	Mollusk	Braun (2019)
Beta-509927	A2	365*	>43500 [#]	>50000	Mollusk	This study
AWI 5105.1.1	A2	374.5*	15745 ± 147 [#]	18491 ± 204	Mixed foram.	This study
AWI 5106.1.1	A1	434.5	13479 ± 125	15513 ± 263	Mollusk	This study

204 [#]age inversion compared to below sampling depth

205 *discarded due to significant age inversion compared to below sampling depth

206 **discarded due to significant age inversion compared to the measurement from different material at the same
207 sampling depth

208

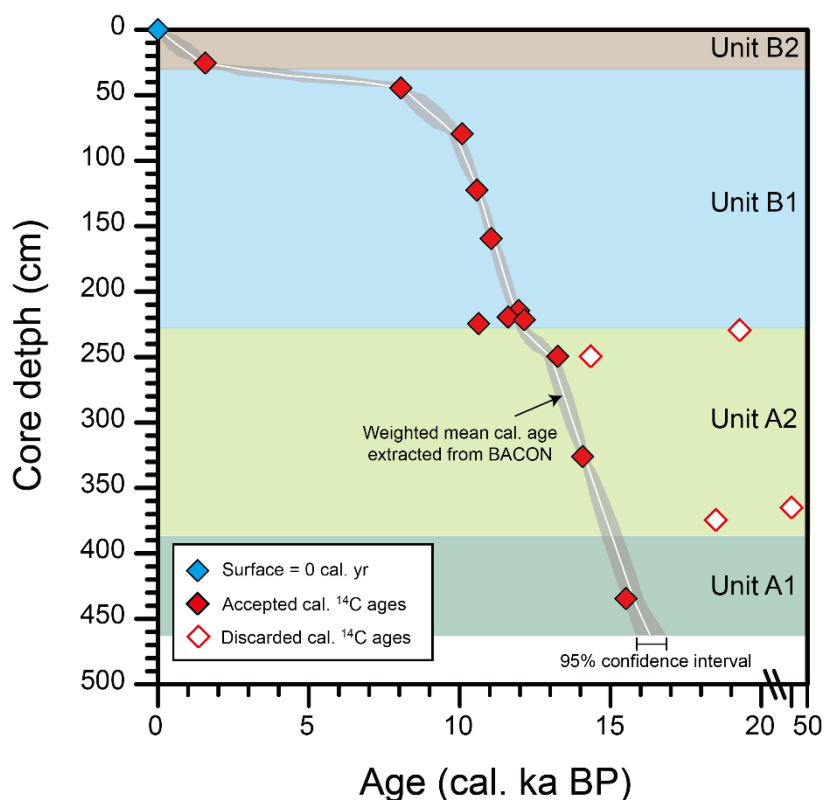


Figure 3. Age model for core HH17-1085. Twelve ^{14}C ages were included (red diamonds) in the BACON model to determine the age-depth relationship (white line, weighted mean age). Four inverted ages were discarded (open diamonds).

209 4.4. *Bulk mineral assemblage analysis*

210 X-ray diffraction pattern analyses were conducted at the University of Bremen. Dried bulk
 211 samples were grounded to a fine powder (<20 μm particle size) and prepared with the Philips
 212 backloading system. The X-ray diffractograms were measured on a Philips X'Pert Pro multipurpose
 213 diffractometer equipped with a Cu-tube ($k\alpha$ 1.541, 45 kV, and 40 mA), a fixed divergence slit of $1/4^\circ$, a
 214 16-sample changer, a secondary Ni filter, and the X'Celerator detector system. The measurements
 215 were performed as a continuous scan from $3-85^\circ 2\theta$, with a calculated step size of $0.016^\circ 2\theta$ (the
 216 calculated time per step was 50 s). Mineral identification was achieved using the Philips software
 217 X'Pert HighScoreTM, and the identification of sheet silicates was performed with the software
 218 MacDiff 4.25 (Petschick et al., 1996). This was followed by a full quantification of the main mineral
 219 assemblages of the bulk fraction via the QUAX full pattern method (c.f., Vogt et al., 2002). A

220 thorough preparation commonly increases the reproducibility of the results; however, the standard
221 deviation given by Moore and Reynolds Jr (1989) of $\pm 5\%$ can be considered a general guideline for
222 mineral groups with $>20\%$ clay fraction. The determination of major none clay minerals can be
223 achieved with better standard deviations ($\pm 1-3\%$; Vogt et al., 2002).

224

225 4.5. *TOC, N_{org} , and $\delta^{13}C_{org}$ measurements*

226 The contents of total organic carbon (TOC) and nitrogen (N_{org}) and the isotopic ratios of
227 organic carbon ($\delta^{13}C_{org}$) were determined using an elemental analyzer (Flash 2000, Thermo Scientific)
228 connected to an isotope ratio mass spectrometer (Delta V, Thermo Scientific) using continuous flow at
229 KOPRI. For the determination of TOC and $\delta^{13}C_{org}$, the bulk sediments were powdered and then
230 treated with 2 M hydrochloric acid for 24 h to eliminate inorganic carbonate. After sufficient rinsing
231 with Milli-Q water (Millipore, $>18.2\text{ M}\Omega\text{ cm}$) and freeze-drying, the TOC contents and $\delta^{13}C_{org}$ were
232 measured. The $\delta^{13}C_{org}$ of each sample is reported in per mil notation relative to the Vienna Pee Dee
233 Belemnite international standard. For the determination of N_{org} , we applied a KBr-KOH solution to
234 the powdered bulk sediments to eliminate inorganic nitrogen, and the residues were used for the
235 analysis (Silva and Bremner, 1966). The analytical precision is within 0.2 %.

236

237 4.6. *Neodymium isotopes analysis*

238 Neodymium isotopic compositions of the authigenic (Fe-oxide rich) and detrital fractions of
239 sediments were determined using a thermal ionization mass spectrometer (TIMS, Triton, Thermo
240 Scientific) at KOPRI. The definitions of authigenic and detrital fractions follow those used by Jang et
241 al. (2020). The authigenic fraction was obtained by leaching the bulk sediment using 0.02 M
242 hydroxylamine hydrochloride in 25 % acetic acid (hereafter, HH solution) at a 1:1 ratio of reagent and
243 sediments for less than 1 h. Following the complete removal of any carbonate and authigenic fractions
244 via exposure to the HH solution for more than 24 h (with a 10:1 ratio of reagent and sediment), the
245 residual detrital fraction, mostly corresponding to the silicate-rich terrigenous material, was isolated.
246 Detrital fractions were then digested using the alkaline fusion method described in Bayon et al.

247 (2009), which ensured the complete dissolution of the silicate minerals.

248 Each fraction was purified by column chromatography using the combination of both TRU
249 (100 μm , Eichrom) and Ln resins (100 μm , Eichrom) following a procedure modified from Pin and
250 Zalduogui (1997). The neodymium isotope ratios were measured using TIMS and then normalized to
251 the $^{144}\text{Nd}/^{146}\text{Nd}$ value of 0.7219 to correct for mass fractionation. Long-term replicate analyses of the
252 JNdi-1 reference solution (0.512110 ± 0.000014 , $n = 12$) agreed well within uncertainty with the
253 reference value of Tanaka et al. (2000), yielding an inferred external reproducibility of 0.3 ϵ_{Nd} units on
254 measured Nd isotopic compositions. Note that the latter value was systematically taken for estimating
255 the analytical uncertainty associated with studied samples unless the internal error during analysis was
256 larger. The measurements of the BHVO-1 certified reference material (0.512972 ± 0.000011 , $n = 3$)
257 were also identical to the literature values within error (e.g., Raczek et al., 2003), confirming the
258 accuracy of the Nd isotopic measurements performed in this study.

259

260 **5. Results**

261 *5.1. Lithostratigraphy*

262 Based on the sediment color, texture, and structure, as well as its physical properties (wet
263 bulk density and magnetic susceptibility), Braun (2019) defined two main lithostratigraphic units in
264 core 1085-GC: a laminated unit from the core base to 228 cm and a massive unit above 228 cm. We
265 name these units as unit A (lower) and unit B (upper) and further sub-divide them depending on their
266 degree of lamination in unit A and bioturbation in unit B (Table 1 and Fig. 2). Lithostratigraphic unit
267 A1, occurring from the bottom of the core to 385 cm, primarily consists of silt-rich and clay-rich mud
268 (mean size: 2.3 to 8.3 μm ; Supplementary Table S1). It has distinct laminations with cyclic alternation
269 of dark reddish-gray (5YR 4/2) and dark-grayish brown layers (10YR 4/2). In this unit, the maximum
270 IRD flux ($> 1 \text{ mm}$) is 5 grains/ $\text{cm}^2 \cdot \text{ka}$ (Fig. 4), and biogenic detritus is sparse. The overlying unit A2,
271 from 385 to 228 cm, is generally similar to unit A1 but comprises darker (2.5YR 4/2) and coarser
272 sediments (4.7 to 9.3 μm ; Supplementary Table S1). The lamination of this unit is blurred and more

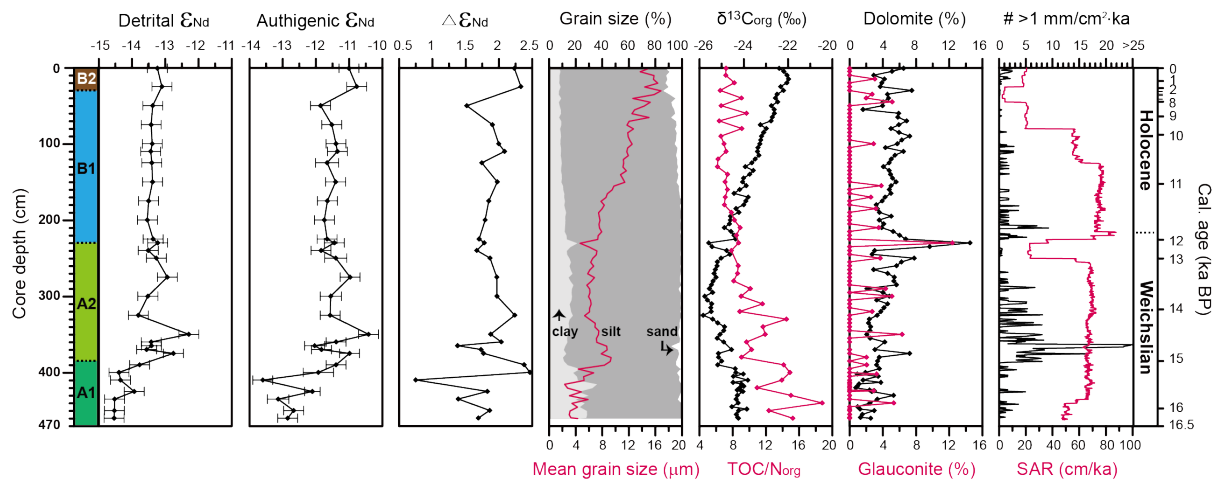


Figure 4. Geochemical proxies, including detrital and authigenic ϵ_{Nd} , $\Delta\epsilon_{Nd}$, grain size distribution, mean grain size, $\delta^{13}C_{org}$, TOC/N_{org} , the contents of dolomite and glauconite, calculated IRD (> 1mm) flux and sediment accumulation rate (SAR) in core HH17-1085-GC. Error bars for ϵ_{Nd} represent $\pm 2\sigma$ uncertainties.

273 poorly defined upwards in the core. A very poorly sorted IRD-rich layer is intercalated in the lower
 274 part of unit A2 (360-370 cm) (Table 1 and Fig. 2), and a distinct pale-brown layer (7.5YR 4/2) is
 275 identified at the top of this unit (228-238 cm). In the IRD-rich layer, IRD flux (> 1mm) exceeds 24
 276 grains/cm²·ka. Stratigraphic unit B1 is defined as the depth interval between 228 and 30 cm and is
 277 composed of massive (dark grayish brown 10YR 4/2 to weak red 2.5YR 4/2) silt-rich mud (7.3 to
 278 15.8 μ m; Supplementary Table S1). There is a coarsening upward trend (Fig. 2), and bioturbation is
 279 generally absent. The top-most unit, B2, is above 30 cm depth and is composed of IRD-rich (Fig. 4),
 280 dark grayish-brown (2.5YR 4/2) sandy mud sediments (13.7 to 16.8 μ m; Supplementary Table S1).
 281 The interval is intensely bioturbated.

282

283 5.2. Chronostratigraphy and sediment accumulation rate

284 The AMS ¹⁴C ages and converted calendar ages are listed in Table 2. The youngest age was
 285 detected at the shallowest depth of 25.5 cm (ca. 1.6 ka BP), while the oldest age was determined at a
 286 depth of 365 cm (> 50 ka BP), where massive clasts up to ~2 cm occur (Fig. 3). The dating results
 287 revealed six ages that were inverted relative to the ages of the corresponding sampled depths below
 288 throughout the core; three represented significant age inversions and were therefore excluded from the

289 determination of the age-depth model (Table 2). Different materials were used for dating at ~249.5
290 cm. They revealed a relatively older age for mollusk shell fragments (ca. 14.3 ka BP) than for
291 corresponding assemblages of mixed benthic foraminifera (ca. 13.2 ka BP); thus, the older age was
292 discarded.

293 The weighted mean values extracted by BACON indicate that the bottom age of core 1085-
294 GC is ca. 16.3 ka BP, and the average sediment accumulation rate was ~28.3 cm/ka (Figs. 3 and 4).
295 This rate is lower than that of core NP94-51, from a nearby site (~42.0 cm/ka; Ślubowska et al.,
296 2005). According to the age model, units A1 and A2 were deposited from ca. 16.3 and 12.1 ka BP,
297 whereas units B1 and B2 were deposited from ca. 12.1 ka BP to the present. The sediment
298 accumulation rate was generally higher between ca. 15.8 and 10.5 ka BP, with a marked decrease
299 observed between ca. 13.0– 12.1 ka BP. There was a stepwise decrease in the sediment accumulation
300 rate after ca. 9.8 ka BP until ca. 5.3 ka BP, when an overall minimum was reached (Fig. 4)(Allaart et
301 al., 2020).

302

303 5.3. Dolomite and glauconite contents

304 The dolomite content ranges from 0.7 to 14.5 %, with an average value of 4.2 % (1σ , $n = 99$)
305 (Supplementary Table S1 and Fig. 4). The abundance of dolomite is generally lower within unit A1
306 (average of 2.3 ± 1.2 %, 1σ , $n = 22$) than in the other units, whereas its variability is largest within
307 unit A2 (average of 4.5 ± 2.6 %, 1σ , $n = 31$) (Fig. 5). A prominent dolomite peak up to 14.5 % occurs
308 in the pale brown layer in the uppermost part of unit A2. This peak corresponds to an abrupt increase
309 in glauconite content to 12.4 %, which is almost 15 times higher than the average glauconite content
310 across the entire core (0.8 ± 1.9 %, 1σ , $n = 31$) (Fig. 4).

311

312 5.4. TOC, N_{org} and $\delta^{13}C_{org}$

313 The overall ranges of TOC and N_{org} are 0.2-1.5 % and 0.02-0.16 %, respectively
314 (Supplementary Table S1). These two parameters strongly correlate with each other ($r = 0.93$, $n = 46$)
315 and generally have largely uniform values within units A1 and A2, gradually increasing towards the

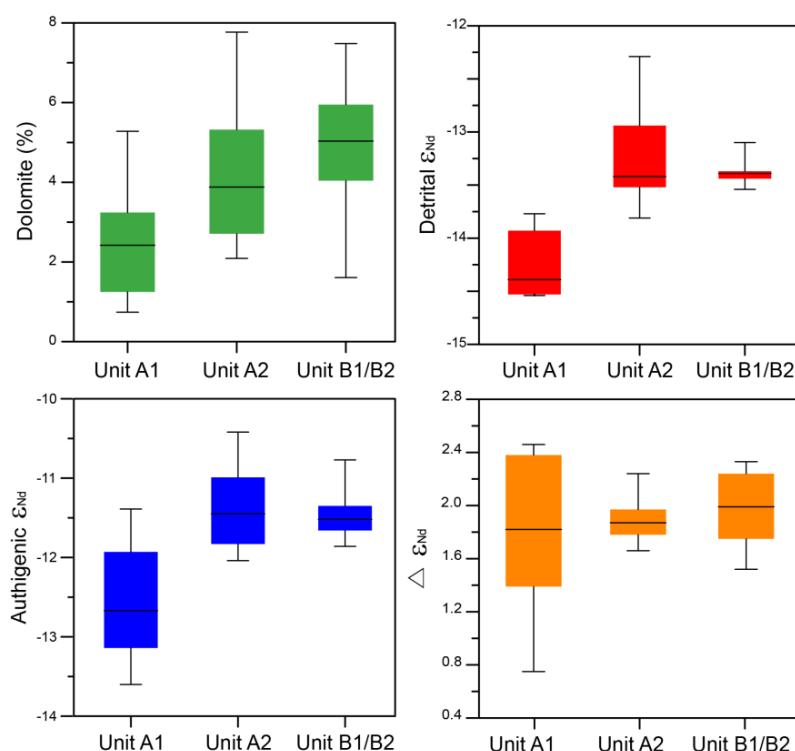


Figure 5. Box and whisker plots of dolomite contents, detrital and authigenic ϵ_{Nd} , and the ϵ_{Nd} differences ($\Delta\epsilon_{Nd}$) within each lithological unit. Note that the exceptional outlier of dolomite within the pale-brown sediments in unit A2 was discarded for the calculation.

316 core-top within units B1 and B2. The TOC/ N_{org} ratios are much lower within units B1 and B2 ($7.5 \pm$
 317 1.0 , 1σ , $n = 23$) than within unit A1 (14.4 ± 2.3 , 1σ , $n = 8$) (Fig. 4). The $\delta^{13}C_{org}$ values show a
 318 decreasing trend from the bottom (-24.2 ‰) to the middle of stratigraphic unit B1 (down to -25.8 ‰)
 319 and then a gradually increasing trend upward (up to -22.0 ‰) (Fig. 4).

320

321 5.5. Detrital and authigenic ϵ_{Nd}

322 The detrital and authigenic ϵ_{Nd} values of core 1085-GC range from -14.5 to -12.3 ($-13.6 \pm$
 323 0.5 , 1σ , $n = 29$) and -13.6 to -10.4 (-11.7 ± 0.7 , 1σ , $n = 29$), respectively, throughout the core
 324 (Supplementary Table S3 and Fig. 4). Both ϵ_{Nd} values are generally well correlated ($r = 0.87$, $n = 29$).
 325 Less radiogenic ϵ_{Nd} values characterize unit A1, with a minimum of -14.5 (-13.6) for the detrital
 326 (authigenic) components and a generally upward increasing trend (Fig. 5). In unit A2, the background
 327 ϵ_{Nd} values for detrital and authigenic components are ~ -13.8 and -12.0 , respectively, but radiogenic ϵ_{Nd}
 328 peaks of -12.8 and -11.0 , respectively, occur in this sediment interval in association with the presence

329 of episodic IRD. In unit B1, the ϵ_{Nd} values of both components are relatively uniform without any
 330 particular fluctuation, showing mean values of -13.4 ± 0.1 for detrital (1σ , $n = 9$) and -11.6 ± 0.2 for
 331 authigenic (1σ , $n = 9$) components. In unit B2, the detrital and authigenic ϵ_{Nd} values are relatively
 332 high, up to -13.1 and -10.8 , respectively, with larger variability in authigenic ϵ_{Nd} .

333

334 **6. Discussion**

335 *6.1. Sediment provenance interpretation*

336 Detrital ϵ_{Nd} values provide a powerful means for identifying any downcore variation in
 337 sediment provenance in our study areas, including Woodfjorden, Wijdefjorden, Nordaustlandet and
 338 the Kara Sea shelf. The ϵ_{Nd} values from the literature for outcrops in Woodfjorden, Wijdefjorden and
 339 Nordaustlandet and sea-ice rafted sediments on the Kara Sea shelf can be divided into four groups: 1)
 340 unradiogenic (low) ϵ_{Nd} values from eastern Wijdefjorden ($-25.4 < \epsilon_{Nd} < -18.6$; Johansson et al., 1995;
 341 Johansson and Gee, 1999), 2) intermediate ϵ_{Nd} values from Woodfjorden and western Wijdefjorden
 342 ($\epsilon_{Nd} \sim -13.6$ for the so-called Devonian Old Red Sandstone from Jang et al., 2020), 3) the most
 343 radiogenic (high) ϵ_{Nd} compositions from Nordaustlandet ($-13.2 < \epsilon_{Nd} < -7.4$; Johansson et al., 2000;
 344 Johansson et al., 2002) and 4) the Kara Sea shelf ($\epsilon_{Nd} \sim -8.9$; Tütken et al., 2002) (Fig. 1C). Note that
 345 the catchment area of Lomfjorden on northeastern Ny-Friesland is primarily dominated by Permian
 346 rocks (Blomeier et al., 2011), implying different ϵ_{Nd} values from those of eastern Wijdefjorden where
 347 Proterozoic to lower Silurian metamorphic rocks predominate (Dallmann, 2015) (Fig. 1C). We
 348 assume that this provenance is characterized by a relatively radiogenic ϵ_{Nd} based on the recent
 349 measurements of detrital ϵ_{Nd} from Permian rocks collected near Isfjorden and Kongsfjorden in
 350 Svalbard ranging from -11.6 to -8.5 (Jang et al., 2020) (Fig. 1C).

351 The sediment mineral assemblages represent an additional proxy for identifying sediment
 352 provenance, which complements the use of Nd isotopes. In this study, the presence of dolomite in the
 353 sediments can be unambiguously attributed to detrital inputs from dolostones outcropping in the
 354 Neoproterozoic basement on southwestern Nordaustlandet (Kunzmann et al., 2015) and/or from the
 355 Permian sedimentary sequence in northeastern Ny-Friesland (Blomeier et al., 2011). Detrital input

356 from both sources would be likely to be accompanied by an increase in ϵ_{Nd} , although differing from
357 other radiogenic but dolomite-poor sediment sources derived from, for instance, the Kara Sea shelf.
358 On the basis that rises in detrital ϵ_{Nd} are generally associated with increases in dolomite (Figs. 4 and
359 5), we infer that the Kara Sea shelf does not represent a dominant source of sediment in the studied
360 area. Considering the location of the two potential sources considered in this study (Nordaustlandet
361 and northeastern Ny-Friesland), together with water circulation patterns and past ice-flow directions
362 (e.g., Batchelor et al., 2011; Dowdeswell et al., 2010; Hormes et al., 2011), the Hinlopen Strait
363 represents the most plausible pathway for dolomite delivery to the core site. Therefore, we hereafter
364 refer to both sources as ‘the Hinlopen-source’. The supply of detrital sediments from the Hinlopen-
365 source is supported by an increase in the detrital ϵ_{Nd} value of the surface sediments of up to 2.7
366 compared with those in inner Wijdefjorden (Jang et al., 2020) (Fig. 1).

367 Likewise, the presence of glauconite can be traced back to the terrestrial input from the
368 Carboniferous and Permian sedimentary rocks in the Wahlenbergfjorden catchment area in
369 southwestern Nordaustlandet where glauconite-rich beds are common (e.g., Bond et al., 2018;
370 Lauritzen, 1981). Glauconite is also present in small amounts as streaks and patches within the
371 dolomite sequence in northeastern Ny-Friesland (Fortey and Bruton, 1973), and thus this area could
372 be a minor source.

373

374 6.2. *Glacimarine sedimentary and environmental changes in northern Svalbard*

375 6.2.1. Late Weichselian – early deglaciation (unit A1, 16.3–15.0 ka BP)

376 The lowermost unit, A1, characterized by fine-grained laminations, is suggested to have been
377 deposited in an ice-proximal setting that prevailed between ca. 16.3 and 15.0 ka BP (hereafter referred
378 to as the early deglaciation period) (Table 1 and Fig. 2). Fine-grained laminated glacimarine
379 sediments in Svalbard fjords typically correspond to depositional environments associated with the
380 settling of meltwater plume-derived suspended particles in ice-proximal environments (e.g., Elverhøi
381 et al., 1995; Forwick and Vorren, 2009; Forwick et al., 2010). During the retreat of the ice margin
382 (e.g., tidewater glaciers and/or ice sheets), the mixing of meltwater with ambient seawater initiates a

383 buoyant plume from which the settling of suspended particles is size-dependent, generating laminated
384 structures (review in Ó Cofaigh and Dowdeswell, 2001). In full agreement with this interpretation, we
385 suggest that the sediment deposited during the early deglaciation period derived primarily from
386 meltwater plumes emanating from the retreating marine-terminating margin of the ice sheet that
387 existed on the continental shelf off northern Svalbard. Our data indicate that the ice extent at
388 approximately 16 ka BP was slightly smaller than that proposed by Hughes et al. (2016), who showed
389 that the SBIS nearly covered Svalbard, including our core site, at ca. 16 ka BP (Fig. 6A) before
390 retreating towards the mouth of Wijdefjorden and Woodfjorden during the early deglaciation. Light
391 $\delta^{13}\text{C}_{\text{org}}$ values and high TOC/ N_{org} ratios indicate organic matter of predominantly terrestrial origins in
392 Svalbard fjord sediments (Knies and Martinez, 2009; Winkelmann and Knies, 2005) (Fig. 4) most
393 likely delivered via subglacial conduits at the base of the SBIS. Such subglacial pathways could have
394 transported land-derived material and re-mobilized glacial marine sediments to the adjacent ice margin.

395 In this study, our suite of provenance proxies suggests that the sediment deposited at the core
396 location during the early deglaciation period was mostly derived from the Devonian Old Red
397 Sandstone, which is dominant in the catchment areas of Woodfjorden and Andrée Land to the west of
398 Wijdefjorden. The detrital ϵ_{Nd} values of the sediments (-14.3 ± 0.3 , 1σ , $n = 7$) are slightly less
399 radiogenic than those of the Old Red sandstone (-13.6 ± 0.3 from Jang et al., 2020) but very similar to
400 those for core-top sediments at the mouth of Wijdefjorden (-14.2 ± 0.2 from Jang et al., 2020) and
401 central Woodfjorden (-14.1 ± 0.2 from Jang et al., 2020) (Fig. 1C). This origin is further supported by
402 the overall reddish color of the sediment, which is consistent with the Devonian Old Red Sandstone
403 (Blomeier et al., 2003a; Blomeier et al., 2003b; Rasmussen and Thomsen, 2013). The mixing of
404 detrital sediment sources from east Wijdefjorden and Nordaustlandet, characterized by less and more
405 radiogenic ϵ_{Nd} signatures, respectively, could possibly account for the observed ϵ_{Nd} sediment
406 signatures. However, the generally low dolomite contents in core 1085-GC sediments suggest that
407 these sources only acted as minor sediment contributions during this period. Accordingly, we propose
408 that the sediment supply was dominated by input from the western sources, probably reflecting
409 enhanced deglaciation on northwestern Svalbard (Fig. 6A).

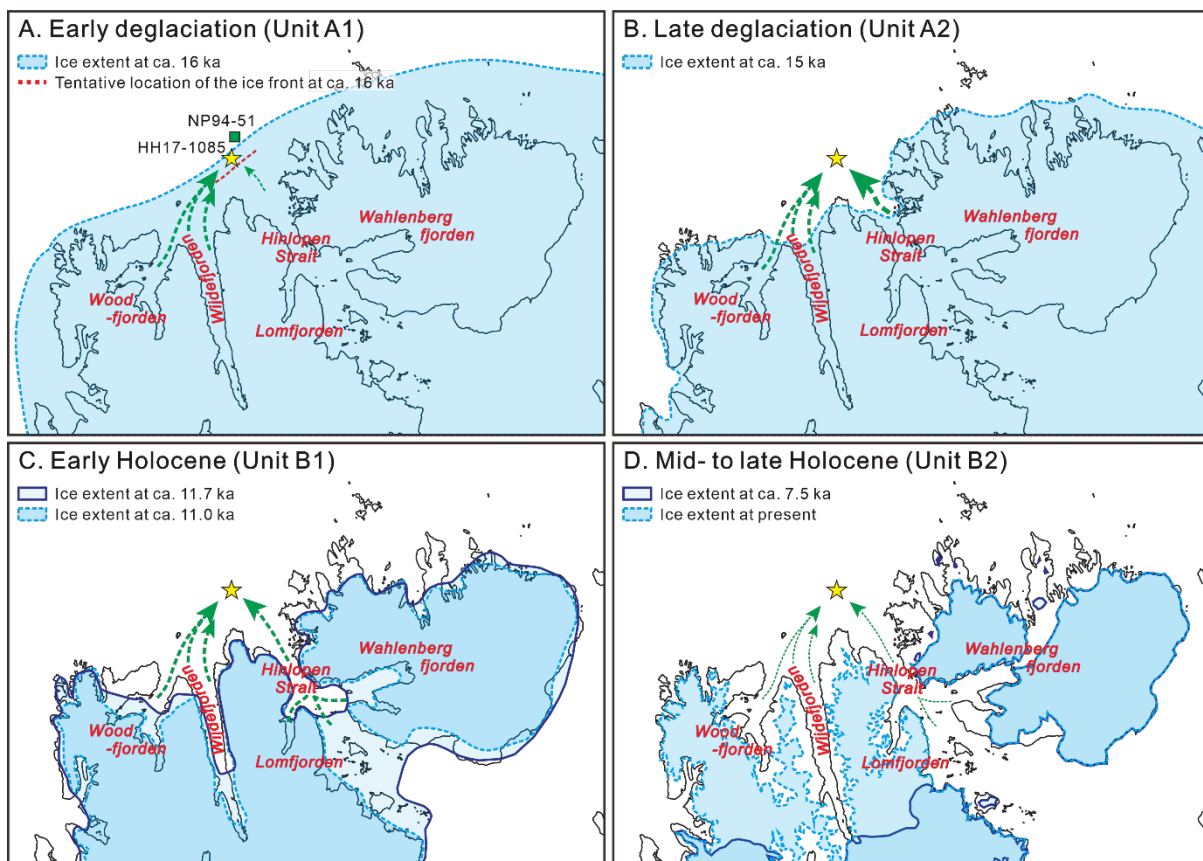


Figure 6. Schematic illustrations of the potential pathways of sediments with estimated ice extents during (A) the early deglaciation, (B) the late deglaciation, (C) the early Holocene, and (D) the middle to late Holocene. The assumed pathways for sediment delivery are marked with green dashed arrows. The estimated extents of the Svalbard-Barents Sea Ice Sheet (SBIS) and land glaciers are generally consistent with previous reconstructions from the most credible DATED-1 timeslices (16 and 15 ka BP; Hughes et al., 2016), the SVALHOLA database (11.7 and 11.0 ka BP; Farnsworth et al., 2020), best-fit model (7.5 ka BP; Fjeldskaar et al., 2018) and satellite images (present; Nuth et al., 2013). However, our data indicate that the ice extent around 16 ka BP terminated further south (red dotted line in Fig. 6A) than suggested by Hughes et al. (2016).

410

411 6.2.2. Late Weichselian – late deglaciation (unit A2, 15.0–12.1 ka BP)

412 The seesaw fluctuations in detrital ϵ_{Nd} values in the deposits between ca. 15.0 and 12.1 ka BP

413 (hereafter referred to as the late deglaciation period) probably reflect the interplay between various

414 sediment sources from Woodfjorden, Wijdefjorden, and Nordaustlandet (Fig. 4). In this context, less

415 radiogenic ϵ_{Nd} values would reflect enhanced detrital contributions from Woodfjorden and416 Wijdefjorden, whereas more radiogenic ϵ_{Nd} values would presumably correspond to inputs from

417 Nordaustlandet (Fig. 6B).

418 The most notable feature of unit A2 is the overall increase in sedimentary ϵ_{Nd} values (Fig. 4).
419 Given the Nd isotopic compositions of the potential sources, the observed ϵ_{Nd} shift towards more
420 radiogenic values can be attributed to enhanced terrestrial inputs from the Hinlopen-source,
421 presumably via northward glacier drainage through the Hinlopen Strait (e.g., Batchelor et al., 2011;
422 Dowdeswell et al., 2010) (Fig. 1). An accompanying increase in dolomite (Fig. 4) supports
423 Nordaustlandet and northeastern Ny-Friesland as potential source regions (compare with Kunzmann
424 et al., 2015). Enhanced sediment supply from the Hinlopen-source was accompanied by the episodic
425 occurrence of IRD (Figs. 2 and 4), suggesting partial break-up of the SBIS on the northeastern margin
426 of Svalbard at ca. 15.0 ka BP (Fig. 6B). Alternatively, the IRD-rich sediments overlying the laminated
427 mud could be interpreted as reflecting the disappearance of sea-ice, which impacts iceberg drift
428 (Kleiber et al., 2000; Ó Cofaigh and Dowdeswell, 2001). However, the observed lack of diatom
429 species at the neighboring site represented by core NP94-51 suggests that sea-ice coverage was
430 extensive at that time (Koç et al., 2002), which rules out this latter hypothesis. Therefore, the
431 transition of the primary provenance from northwestern to northeastern Svalbard implies that the
432 retreat of the SBIS on the northeastern margin of Svalbard started later than that at the northwestern
433 margin. The delayed retreat of the SBIS at the northeastern margin of Svalbard may have been related
434 to the strong subsurface intrusion of warm AW to northern Svalbard during that time (Ślubowska et
435 al., 2005). However, this suggestion remains speculative for the time being and cannot be evaluated
436 until additional quantitative ϵ_{Nd} data from Nordaustlandet become available.

437 The progressive disappearance of laminated sediment at the studied site after the partial
438 break-up of the SBIS along the northeastern margin of Svalbard indicates a gradual transition from
439 ice-proximal to ice-distal glacimarine environments (Ó Cofaigh and Dowdeswell, 2001). Upward
440 decreases in the sand/mud and silt/clay ratios support a progressive increase in the distance between
441 the retreating ice margin and the core location (e.g., Mackiewicz et al., 1984). This finding is
442 consistent with previous studies that documented the ongoing retreat of the SBIS from the northern
443 Svalbard coast into mid-Wijdefjorden, Woodfjorden, and the Hinlopen Strait during the late
444 deglaciation period (Allaart et al., 2020; Bartels et al., 2017; Hughes et al., 2016 and references

445 therein) (compare Fig. 6A with Fig. 6B).

446 The final phase of the deglaciation is marked by the deposition of a pale-brown sediment
447 layer at ca. 12.1 ka, which corresponds to an abrupt increase in dolomite (~14.5 %) and glauconite
448 (~12.4 %) contents at the top of A2 (Fig. 4). These changes in the sediment mineral assemblage
449 indicate sediment input predominantly from the catchment area of Wahlenbergfjorden on
450 southwestern Nordaustlandet with a minor contribution from northeastern Ny-Friesland (see *section*
451 *6.1*). Bartels et al. (2018) reported the occurrence of similar pale-brown sediment in the bottommost
452 part of a core GeoB10831-3 retrieved from inner Wahlenbergfjorden (before ca. 11.3 ka BP) (Fig.
453 1C). Nevertheless, the detrital ϵ_{Nd} values at core 1085-GC (Fig. 4) are less radiogenic than the
454 representative ϵ_{Nd} values of bedrock in western and central Nordaustlandet ($-13.2 < \epsilon_{Nd} < -7.4$;
455 Johansson et al., 2000; Johansson et al., 2002) and northeastern Ny-Friesland ($-11.6 < \epsilon_{Nd} < -8.5$; Jang
456 et al., 2020) (Fig. 1), which could be at least partly attributable to less radiogenic Nd inputs from
457 northwestern detrital sources.

458 The deposition of such a homogenous layer of sediments delivered mainly from SW
459 Nordaustlandet to the continental shelf off northern Svalbard could reflect either rapid retreat/collapse
460 of glaciers, or increased meltwater release. The rapid retreat or collapse of glaciers can lead to the
461 deposition of coarse-grained materials. However, the increase in clay content and absence of IRD in
462 this layer suggest that this layer was caused by a meltwater pulse accompanied by considerable
463 sediment transport rather than by deposition from ice rafting. This pulse could be attributed to a rapid
464 transition from cold conditions during the Younger Dryas, 12.9–11.7 ka BP, to warm conditions
465 (Farnsworth et al., 2020 and references therein). Considering the potential age uncertainty inferred
466 from the younger ^{14}C ages above this layer (10.6 ka BP; Fig. 3), this distinct sediment layer might
467 correspond to the second-largest meltwater pulse MWP-1B reconstructed in Storfjorden at 11.3–11.0
468 ka BP (e.g., Tian et al., 2020), implying ubiquitous glacier melting across Svalbard after the Younger
469 Drays. However, there are several dates providing older ages from shallower core depths (12.1–11.6
470 ka BP; ~15 cm above; Fig. 3); thus, this meltwater pulse more likely reflects a local event.

471

472 6.2.3. Latest Weichselian – Holocene (units B1 & B2, 12.1 ka BP to the present)

473 Unit B1, characterized by the massive fine-grained mud, was deposited in a more distal
474 glacial marine environment between ca. 12.1 and 2.7 ka BP (Allaart et al., 2020; Ó Cofaigh and
475 Dowdeswell, 2001). In the lower part of unit B1, deposited between ca. 12.1 and 9.9 ka BP, the
476 sediment accumulation rate remained considerably high (Fig. 3), suggesting high meltwater discharge
477 during the early Holocene (Farnsworth et al., 2020) (Fig. 6C). Indeed, proxy records show that
478 glaciers on Svalbard experienced massive losses during the early Holocene (Farnsworth et al., 2020,
479 and references therein). This is in accordance with a recent modeling study based on relative sea-level
480 showing the disappearance of all glaciers except for the largest glaciers in Nordaustlandet and eastern
481 Spitsbergen before 7.5 ka BP (Fjeldskaar et al., 2018). This extensive melting of glaciers probably
482 produced large meltwater runoff, resulting in relatively high sediment flux throughout the early
483 Holocene, as recorded in Svalbard fjord sediment cores (Allaart et al., 2020; Bartels et al., 2018;
484 Bartels et al., 2017; Flink et al., 2017; Hald et al., 2004) and at our core site off northern Svalbard.

485 The sediment accumulation rate decreased as the deglaciation proceeded through the middle
486 Holocene (Fig. 4), when glaciers on Svalbard reached their Holocene minimum extent (Farnsworth et
487 al., 2020) (Fig. 6D). In particular, the upper part of unit B1 deposited between ca. 8.0 and 2.7 ka BP is
488 characterized by the lowest sediment accumulation rates in our record, suggesting sediment
489 deficiency, as has been ubiquitously documented for the middle Holocene in other Svalbard cores
490 (e.g., Allaart et al., 2020; Bartels et al., 2017; Flink et al., 2017; Rasmussen and Thomsen, 2014). The
491 reduced sediment accumulation rate at that time likely reflects the gradual reduction/disappearance of
492 glaciers and, as a consequence, the reduced supply of terrestrial material, including fine-grained
493 materials (Fig. 4). The possibility of reduced terrestrial input is indirectly supported by the increased
494 contribution of marine organic matter to the total organic carbon budget at site 1085-GC, as inferred
495 from the high $\delta^{13}\text{C}_{\text{org}}$ and low TOC/ N_{org} values (Fig. 4). On the other hand, the glaciers that re-
496 advanced and/or survived during those times (Farnsworth et al., 2020; Fjeldskaar et al., 2018) could
497 have contributed to an increase in sand content (Fig. 4). Such a sand increase would have been
498 enhanced by the winnowing of bottom currents due to a shallowing of the water depth in response to

499 post-glacial isostatic uplift (Forman et al., 2004).

500 The mean grain size and sand contents are highest in unit B2 deposited after ca. 2.7 ka BP,
501 and the IRD flux in this unit is high (Fig. 4). These characteristics reflect glacier advances (e.g.,
502 Allaart et al., 2020) corresponding to the general cooling in Svalbard during this period (Dowdeswell
503 et al., 2020; Forwick and Vorren, 2009; Hald et al., 2004; Svendsen and Mangerud, 1997). The high
504 sand content during this interval is likely associated with ice-rafting processes. The advances of
505 glaciers on northern Svalbard during the late Holocene would have led to intensified iceberg
506 production (Allaart et al., 2020; Bartels et al., 2017; Ślubowska et al., 2005), delivering coarse-
507 grained sediments to the continental shelf. Sea-ice rafting could have also contributed to the transport
508 of coarse-grained sediments from the shore to the continental shelf. This interpretation is supported by
509 the gradual increase in sea-ice cover at the mouth of Wijdefjorden during the last few millennia
510 (Allaart et al., 2020) and the temporarily enhanced sea-ice cover at NP94-51 during the Little Ice Age
511 (Jernas et al., 2013).

512 During the Holocene, the sediment provenance remained more constant than during the
513 deglaciation, as evidenced by the near-constant detrital ϵ_{Nd} signatures. The detrital ϵ_{Nd} values are
514 generally comparable to those encountered during the final phase of deglaciation, which suggests
515 sediment supply from similar source regions. However, the occurrence of low-to-moderate dolomite
516 and glauconite contents could indicate that reduced sedimentary inputs from southwestern
517 Nordaustlandet contributed to the Hinlopen-source (Fig. 4); this reduced input was probably due to
518 the increase in distance between the glacial source of the sediments and the core site as glaciers
519 retreated.

520

521 6.3. *Application of $\Delta\epsilon_{Nd}$ as a proxy for reconstructing glacial activity in northern Svalbard*

522 The Nd isotopic composition of authigenic iron oxide fractions has been widely used as a
523 proxy for water masses in paleoceanographic studies. The Nd isotopic variations in the leached Fe-
524 oxide fractions of marine sediment records can provide information on past hydrological changes,
525 such as the strength of the Atlantic Meridional Overturning Circulation (e.g., Böhm et al., 2015;

526 Jonkers et al., 2015; Piotrowski et al., 2005; Rutberg et al., 2000), dense water formation (e.g., Jang et
527 al., 2017) and meltwater discharge events (e.g., Jang et al., 2013). The erosive behavior of ice sheets
528 and glaciers on continental masses can also release substantial amounts of dissolved Fe, leading to
529 subsequent co-precipitation of nanoparticulate Fe oxides (review in Wadham et al., 2019). Recent
530 studies have shown that weathering processes in catchments hosting sedimentary rocks (such as in
531 Svalbard) could be accompanied by the release of dissolved Nd isotopic signatures (and associated Fe
532 oxide phases) being significantly more radiogenic than the corresponding detrital sediment fraction
533 (Bayon et al., 2020; Hindshaw et al., 2018; Jang et al., 2020). The application of this new ϵ_{Nd}
534 approach to Svalbard fjord sediments showed that the analysis of paired detrital and authigenic
535 fractions could provide useful information on the degree of incongruent chemical weathering and
536 associated glacial evolution (e.g., Jang et al., 2020).

537 At the site of core 1085-GC, authigenic ϵ_{Nd} values are strongly correlated with corresponding
538 detrital ϵ_{Nd} values ($r = 0.87$, $n = 29$) (Fig. 4), suggesting that the dissolved terrestrial input exerts a
539 strong influence on the ϵ_{Nd} composition of leached Fe oxide phases. As proposed by Jang et al. (2020),
540 this correlation in Svalbard fjord sediments suggests that meltwater releases are accompanied by
541 substantial delivery of dissolved Fe and rare earth elements derived from the chemical weathering of
542 rocks hosted in glaciated catchments, thereby leading to subsequent co-precipitation of abundant Fe-
543 oxyhydroxide phases in the water column. Alternatively, the presence of ancient preformed Fe-oxides
544 delivered by meltwater discharge and sea-ice entrainment could also dominate the leached ϵ_{Nd} signal
545 extracted from the studied fjord sediments (Bayon et al., 2004; Bayon et al., 2020; Werner et al.,
546 2014). However, the authigenic ϵ_{Nd} values (from -13.6 to -11.4) obtained for the early deglaciation
547 period are considerably less radiogenic than the ϵ_{Nd} value of leached (preformed) phases from the
548 Devonian Old Red Sandstones (-10.8 from Jang et al., 2020), and those retrieved from Kara Sea shelf
549 sediments (-4.2 from Chen et al., 2012; -5.9 from Haley and Polyak, 2013), suggesting that these
550 latter sediment sources were not important sources of ‘terrestrial’ preformed Fe oxides in Svalbard
551 fjords.

552 Since the strong correlation between authigenic and detrital ϵ_{Nd} values may be a coincidence,

553 we evaluated the possibility that both ϵ_{Nd} signatures originate from separate sources. In the Fram
554 Strait, the ϵ_{Nd} variability in sedimentary authigenic fractions has been interpreted as reflecting changes
555 in the relative influence of AW (-13.2 to -13.0 from Teschner et al., 2016) and comparatively more
556 radiogenic ArW (-9.9 from Laukert et al., 2017) (Maccali et al., 2013; Rahaman et al., 2020; Werner
557 et al., 2014). On this basis, the radiogenic excursion for authigenic ϵ_{Nd} identified at the site of core
558 1085-GC during the late deglaciation period (ca. 15–14 ka BP) could possibly be explained by a
559 stronger influence of the ArW offshore northern Svalbard. However, the increase in *C. neoteretis* at
560 the neighboring site represented by core NP94-51 indicates a stronger inflow of relatively warm AW
561 (Ślubowska et al., 2005), suggesting that the observed authigenic ϵ_{Nd} excursion towards radiogenic
562 values cannot be interpreted as a re-organization of ocean circulation patterns. Furthermore, while the
563 increase in authigenic ϵ_{Nd} observed at the studied site corresponding to the early stage of the late
564 Holocene could be attributed partly to reduced inflow of the AW (Ślubowska-Woldengen et al., 2007;
565 Ślubowska et al., 2005; Werner et al., 2014), this hypothesis disagrees with paleoceanographic
566 reconstructions indicating the increased inflow of AW during the latter stage of the late Holocene
567 (Rasmussen et al., 2007; Ślubowska-Woldengen et al., 2007; Ślubowska et al., 2005). Collectively, the
568 measured authigenic ϵ_{Nd} signatures in leached Fe-oxide fractions suggest a terrestrial origin sourced
569 from subglacial to deglacial meltwater.

570 On this basis, we infer that the radiogenic authigenic ϵ_{Nd} peak of -10.8 (and the associated
571 high $\Delta\epsilon_{Nd}$ value) that occurred at ca. 1.4 ka BP (Fig. 4) reflects an increase in the glacier extent on
572 Svalbard during the late Holocene (Dowdeswell et al., 2020; Kempf et al., 2013; Martín-Moreno et
573 al., 2017) (Fig. 7B). At that time, the increased glacial abrasion induced by the growth of glaciers
574 would have provided freshly exposed rock substrates and would have been followed by the
575 preferential dissolution of easily dissolvable rock minerals during chemical weathering, resulting in an
576 enhanced isotopic decoupling of Nd between solutes and source rocks, i.e., a higher $\Delta\epsilon_{Nd}$ (Jang et al.,
577 2020) (Fig. 7A). Similar increases in $\Delta\epsilon_{Nd}$ during the late Holocene have been found in sediment
578 cores retrieved from Woodfjorden (HH12-964) and Dicksonfjorden (HH16-1202) (Jang et al., 2020)
579 (for locations, see Fig. 1). While the $\Delta\epsilon_{Nd}$ values of core 1085-GC are slightly lower than those for

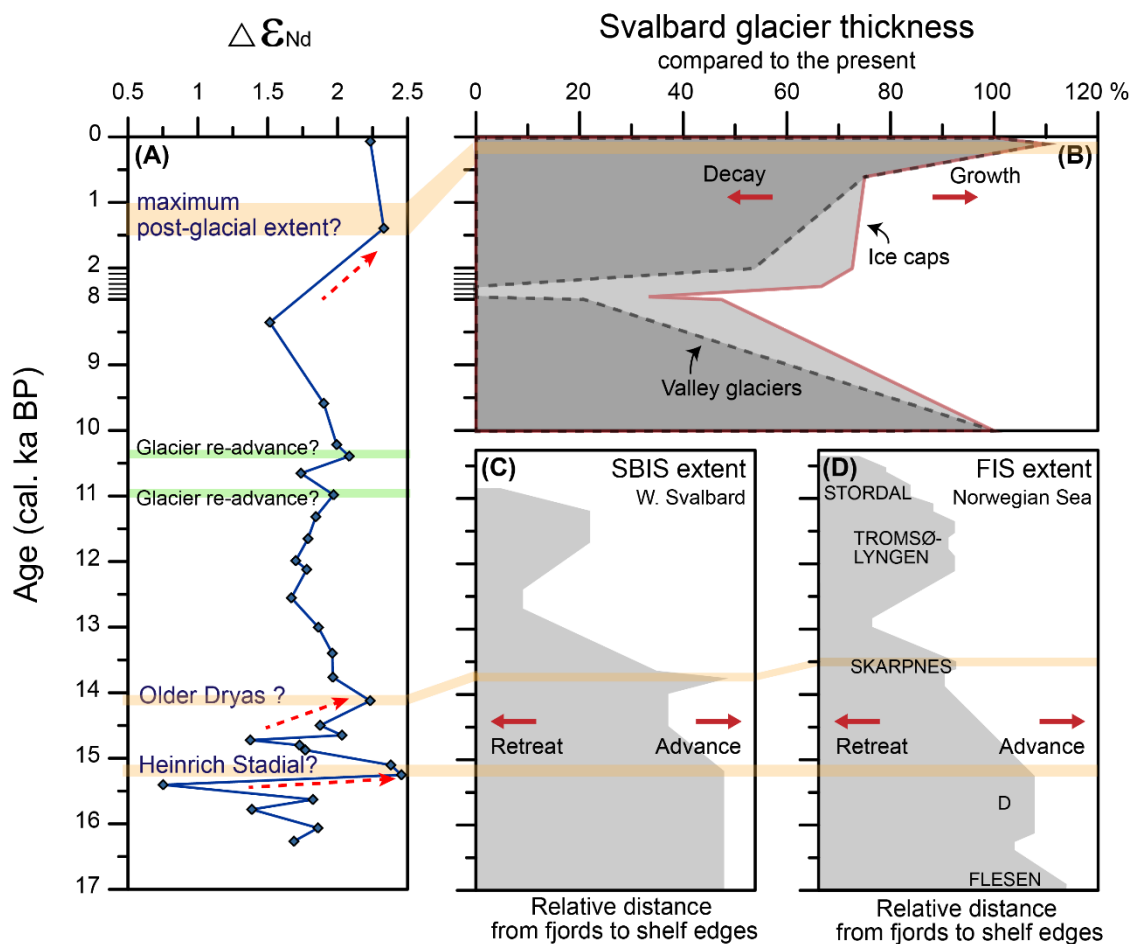


Figure 7. (A) Differences between the authigenic and detrital ϵ_{Nd} values ($\Delta\epsilon_{Nd}$) at the site of core HH17-1085-GC, (B) the modeled extent of Svalbard glaciers (Fjeldskaar et al., 2018), and the reconstructed extents of (C) the Svalbard-Barents Sea Ice Sheet (SBIS) in western Svalbard (Ebbesen et al., 2007; Elverhøi et al., 1995; Svendsen et al., 1996) and (D) the Fennoscandian Ice Sheet (FIS) in the Andfjord-Vågsfjord area in northern Norway (Vorren and Plassen, 2002). Three $\Delta\epsilon_{Nd}$ peaks beyond the general uncertainty (~ 0.5 units) calculated by Monte-Carlo simulation (2σ , $n = 10,000$) (dashed red arrows) are marked by light orange bars and correlate with the glacial instability. Light green bars indicate minor $\Delta\epsilon_{Nd}$ peaks, which may reflect glacier re-advances during the early Holocene. Five major glacial events for FIS are marked within the gray shaded area in (D).

580 two other nearby sites investigated by Jang et al. (2020), all records display a similar temporal

581 evolution during the late Holocene, suggesting very similar glacial histories at that time.

582 Aside from the high $\Delta\epsilon_{Nd}$ values during the late Holocene, an outstanding feature of our

583 results is the seesaw fluctuations displayed by authigenic ϵ_{Nd} during the early deglaciation ($-12.5 \pm$

584 0.8 , 1σ , $n = 7$) (Fig. 4). Detrital ϵ_{Nd} values were almost constant (-14.3 ± 0.3 , 1σ , $n = 7$) during this

585 period; thus, these fluctuations most likely indicate variations in the degree of Nd isotopic decoupling

586 in response to abruptly changing glacial activity and associated chemical weathering patterns. The

587 maximum $\Delta\epsilon_{Nd}$ values observed at ca. 15.2 ka BP could reflect pronounced ice sheet instability at that
588 time associated with the incipient stage of ice sheet recession as recorded in the cores from offshore
589 western Svalbard (Ebbesen et al., 2007; Elverhøi et al., 1995; Jessen et al., 2010; Svendsen et al.,
590 1996) (Fig. 7C) and from sites offshore northern Norway (Vorren and Plassen, 2002) (Fig. 7D). The
591 major recession of ice sheets (e.g., Hogan et al., 2017) or re-advances (e.g., the D-event in the
592 European Arctic; Vorren and Plassen, 2002) probably supplied substantial fresh rock substrates
593 available for intensifying the weathering of rock-forming minerals and the release of radiogenic
594 isotopic signatures. Following an early stage characterized by intense incongruent weathering
595 processes under unstable ice sheet conditions, the $\Delta\epsilon_{Nd}$ signal would have returned smaller values as
596 chemical weathering becomes more congruent (e.g., Jang et al., 2020; Sűfke et al., 2019). Likewise,
597 the subsequent increase in $\Delta\epsilon_{Nd}$ observed during the late deglaciation (ca. 14.1 ka BP; Fig. 7A) would
598 be related to significant ice sheet instability, perhaps in response to the increase in the Atlantic inflow
599 (Ślubowska et al., 2005). This event could have occurred slightly after the Older Dryas period when
600 the glacial re-advance was short-lived, as documented in western Svalbard (Ebbesen et al., 2007;
601 Elverhøi et al., 1995; Svendsen et al., 1996) (Fig. 7C) and the European Arctic regions (the Skarpnes-
602 event; Vorren and Plassen, 2002) (Fig. 7D).

603 The results of our application of Nd isotopes in leached authigenic fractions suggest that the
604 recession of glaciers on Svalbard progressed through a series of abrupt episodes of glacial
605 retreat/advance rather than occurring gradually throughout the deglaciation period. The deglaciation
606 of northern Svalbard was interrupted at least twice by short-term periods of glacial advances, similar
607 to what has occurred in western Svalbard (Ebbesen et al., 2007; Elverhøi et al., 1995; Svendsen et al.,
608 1996) and the European Arctic (Vorren and Plassen, 2002). The moderate increases in $\Delta\epsilon_{Nd}$ (Fig. 7A)
609 may be synchronous with glacier re-advances during the early Holocene (Farnsworth et al., 2020 and
610 references therein); however, we found no $\Delta\epsilon_{Nd}$ peak during the middle Holocene when glacier re-
611 advances occurred (Baeten et al., 2010; Forwick et al., 2010; Jang et al., 2020; Svendsen and
612 Mangerud, 1997; van der Bilt et al., 2015) (Fig. 8), probably due to sediment starvation at the site of
613 core 1085-GC (Fig. 4).

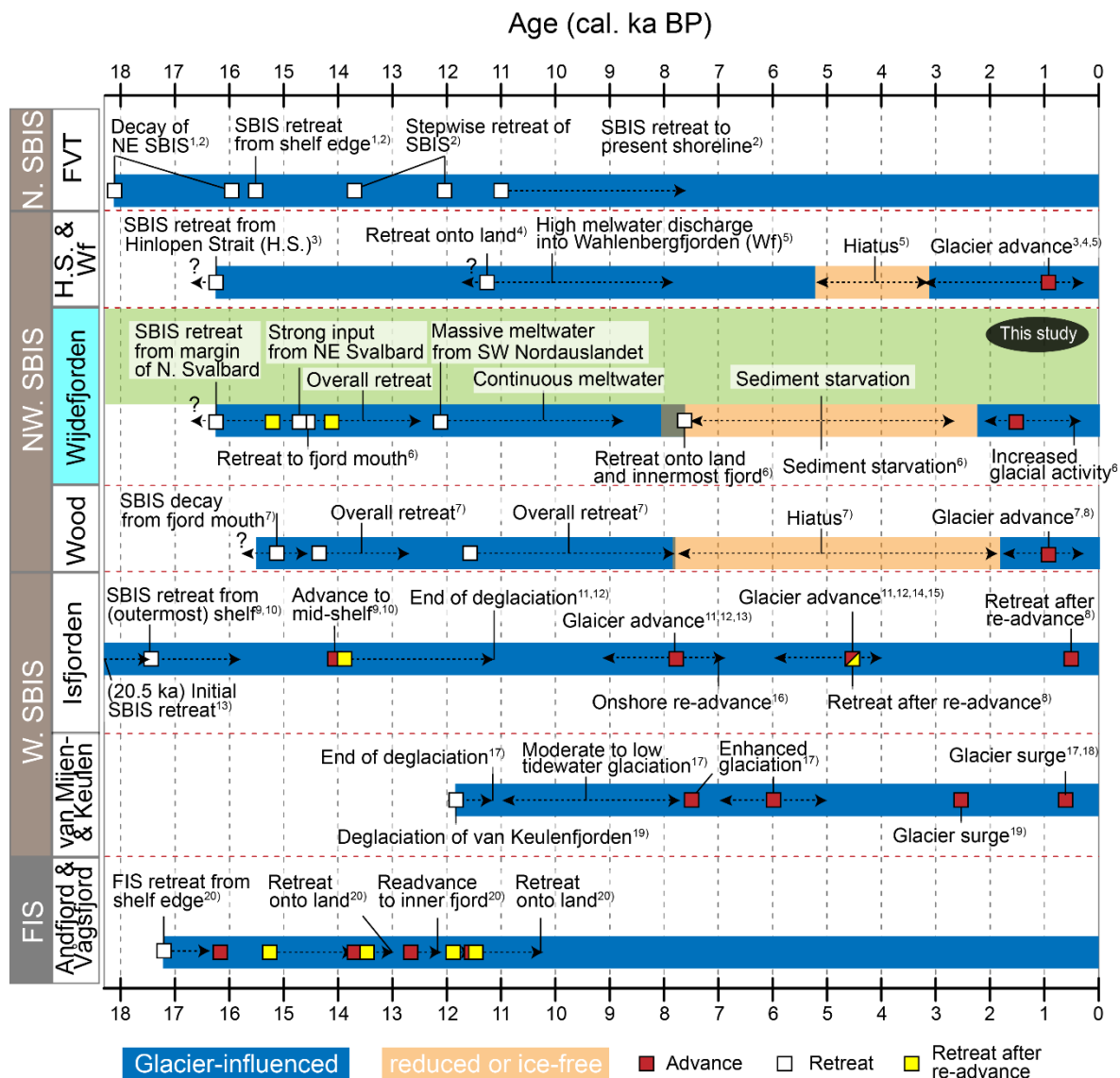


Figure 8. Suggested timeline for the glacial history of northern Svalbard since the last deglaciation. Our results were compared with previous observations from the Franz Victoria Trough (FVT), Hinlopen Strait (H.S.), Wahlenbergfjorden (Wf), Wijdefjorden, Woodfjorden, and Isfjorden in Svalbard and Andfjord and Vågsfjord in Norway. References: ¹Knies et al. (2001), ²Kleiber et al. (2000), ³Koç et al. (2002), ⁴Flink et al. (2017), ⁵Bartels et al. (2018), ⁶Allaart et al. (2020), ⁷Bartels et al. (2017), ⁸Jang et al. (2020), ⁹Svendsen et al. (1996), ¹⁰Elverhøi et al. (1995), ¹¹Forwick and Vorren (2009), ¹²Baeten et al. (2010), ¹³Jessen et al. (2010), ¹⁴Svendsen and Mangerud (1997), ¹⁵Forwick et al. (2010), ¹⁶Forwick and Vorren (2007), ¹⁷Hald et al. (2004), ¹⁸Hald et al. (2001), ¹⁹Kempf et al. (2013), ²⁰Vorren and Plassen (2002)

614

615 **7. Conclusion**

616 Multi-proxy analyses of sediment core 1085-GC from the continental margin offshore

617 northern Svalbard, including the novel use of Nd isotopes in both detrital and authigenic fractions as

618 tracers of glacial weathering, provide new constraints on the dynamics of the last SBIS and glaciers
619 during and after the last deglaciation. Changing sediment provenance and chemical weathering signals
620 indicate that the SBIS probably persisted longer on the northeastern margin of Svalbard than on the
621 northwestern margin and that the deglaciation period in northern Svalbard was punctuated by at least
622 two glacier re-advances at ca. 15.2 and 14.1 ka BP (Fig. 8). This stepwise deglaciation correlates with
623 reconstructions from western Svalbard and northern Norway (Fig. 8), implying that the pronounced
624 large-scale ice sheet dynamics in Svalbard and Fennoscandia were synchronous during the last
625 deglaciation. Glaciers on northern Svalbard underwent changes in extent during the Holocene,
626 including major retreats during the early Holocene and re-advances during the late Holocene. Our
627 study underlines the potential of employing Nd isotopes in both authigenic and detrital fractions for
628 reconstructing the evolution of past ice sheets and glacier activity.

629

630 **Data Availability**

631 The data are available within the paper and its supplementary information files.

632

633 **Acknowledgments**

634 This study was supported mainly by the Basic Core Technology Development Program for
635 the Oceans and the Polar Regions (NRF-2015M1A5A1037243) and the Basic Science Research
636 Program (2017R1A6A3A01076729) from the NRF funded by MSIT, South Korea. We would like to
637 thank S. D. Hur, Y. Han, C. Han, J. Baek, and C. Brice for helping with the instrumental analysis and
638 D. Kim, K. Park, and Y. Son for laboratory assistance. Furthermore, we would like to thank the
639 captain and crew of *R/V Helmer Hanssen* during the 2nd Korea-Norway joint cruise and the other
640 cruise participants for their supporting the core sampling during the cruise.

641

642 **References**

643 Allaart, L., Müller, J., Schomacker, A., Rydningen, T.A., Håkansson, L., Kjellman, S.E., Mollenhauer,
644 G., Forwick, M., 2020. Late Quaternary glacier and sea-ice history of northern Wijdefjorden,

- 645 Svalbard. *Boreas*, doi.org/10.1111/bor.12435.
- 646 Baeten, N.J., Forwick, M., Vogt, C., Vorren, T.O., 2010. Late Weichselian and Holocene sedimentary
647 environments and glacial activity in Billefjorden, Svalbard. *Geol. Soc. Lond., Spec. Publ.* 344,
648 207-223.
- 649 Bartels, M., Titschack, J., Fahl, K., Stein, R., Hebbeln, D., 2018. Wahlenbergfjord, eastern Svalbard: a
650 glacier-surrounded fjord reflecting regional hydrographic variability during the Holocene?
651 *Boreas* 47, 1003-1021.
- 652 Bartels, M., Titschack, J., Fahl, K., Stein, R., Seidenkrantz, M.-S., Hillaire-Marcel, C., Hebbeln, D.,
653 2017. Atlantic Water advection vs. glacier dynamics in northern Spitsbergen since early
654 deglaciation. *Clim. Past* 13, 1717-1749.
- 655 Batchelor, C.L., Dowdeswell, J.A., Hogan, K.A., 2011. Late Quaternary ice flow and sediment delivery
656 through Hinlopen Trough, Northern Svalbard margin: Submarine landforms and depositional
657 fan. *Mar. Geol.* 284, 13-27.
- 658 Bayon, G., Barrat, J.A., Etoubleau, J., Benoit, M., Bollinger, C., Révillon, S., 2009. Determination of
659 rare earth elements, Sc, Y, Zr, Ba, Hf and Th in geological samples by ICP-MS after Tm addition
660 and alkaline fusion. *Geostand. Geoanal. Res.* 33, 51-62.
- 661 Bayon, G., German, C.R., Burton, K.W., Nesbitt, R.W., Rogers, N., 2004. Sedimentary Fe-Mn
662 oxyhydroxides as paleoceanographic archives and the role of aeolian flux in regulating oceanic
663 dissolved REE. *Earth Planet. Sci. Lett.* 224, 477-492.
- 664 Bayon, G., Lambert, T., Vigier, N., De Deckker, P., Freslon, N., Jang, K., Larkin, C.S., Piotrowski, A.M.,
665 Tachikawa, K., Thollon, M., Tipper, E.T., 2020. Rare earth element and neodymium isotope
666 tracing of sedimentary rock weathering. *Chem. Geol.* 553, 119794.
- 667 Berben, S.M., Husum, K., Navarro-Rodriguez, A., Belt, S.T., Aagaard-Sørensen, S., 2017. Semi-
668 quantitative reconstruction of early to late Holocene spring and summer sea ice conditions in
669 the northern Barents Sea. *J. Quaternary Sci.* 32, 587-603.
- 670 Blaauw, M., Christen, J.A., 2011. Flexible paleoclimate age-depth models using an autoregressive
671 gamma process. *Bayesian Anal.* 6, 457-474.

- 672 Blomeier, D., Dustira, A., Forke, H., Scheibner, C., 2011. Environmental change in the Early Permian
673 of NE Svalbard: from a warm-water carbonate platform (Gipshuken Formation) to a temperate,
674 mixed siliciclastic-carbonate ramp (Kapp Starostin Formation). *Facies* 57, 493-523.
- 675 Blomeier, D., Wisshak, M., Dallmann, W., Volohonsky, E., Freiwald, A., 2003a. Facies analysis of the
676 Old Red Sandstone of Spitsbergen (Wood Bay Formation): reconstruction of the depositional
677 environments and implications of basin development. *Facies* 49, 151-174.
- 678 Blomeier, D., Wisshak, M., Joachimski, M., Freiwald, A., Volohonsky, E., 2003b. Calcareous, alluvial
679 and lacustrine deposits in the Old Red Sandstone of central north Spitsbergen (Wood Bay
680 Formation, Early Devonian). *Norw. J. Geol.* 83, 281-298.
- 681 Blott, S.J., Pye, K., 2001. GRADISTAT: a grain size distribution and statistics package for the analysis
682 of unconsolidated sediments. *Earth Surf. Proc. and Land.* 26, 1237-1248.
- 683 Böhm, E., Lippold, J., Gutjahr, M., Frank, M., Blaser, P., Antz, B., Fohlmeister, J., Frank, N., Andersen,
684 M., Deininger, M., 2015. Strong and deep Atlantic meridional overturning circulation during the
685 last glacial cycle. *Nature* 517, 73-76.
- 686 Bond, D.P., Blomeier, D.P., Dustira, A.M., Wignall, P.B., Collins, D., Goode, T., Groen, R.D., Buggisch,
687 W., Grasby, S.E., 2018. Sequence stratigraphy, basin morphology and sea-level history for the
688 Permian Kapp Starostin Formation of Svalbard, Norway. *Geol. Mag.* 155, 1023-1039.
- 689 Braun, C., 2019. Late Weichselian and Holocene glacier dynamics and sedimentary processes in and
690 north of the Wijdefjorden-Austfjorden fjord system, north Spitsbergen. The Arctic University of
691 Norway.
- 692 Chen, T.-Y., Frank, M., Haley, B.A., Gutjahr, M., Spielhagen, R.F., 2012. Variations of North Atlantic
693 inflow to the central Arctic Ocean over the last 14 million years inferred from hafnium and
694 neodymium isotopes. *Earth Planet. Sci. Lett.* 353, 82-92.
- 695 Cottier, F., Tverberg, V., Inall, M., Svendsen, H., Nilsen, F., Griffiths, C., 2005. Water mass modification
696 in an Arctic fjord through cross-shelf exchange: The seasonal hydrography of Kongsfjorden,
697 Svalbard. *J. Geophys. Res. Oceans* 110, C12005.
- 698 Curry, J.A., Schramm, J.L., Ebert, E.E., 1995. Sea ice-albedo climate feedback mechanism. *J. Climate*

- 699 8, 240-247.
- 700 Dallmann, W.K., 2015. Geoscience atlas of Svalbard. Norsk Polarinst. Tromsø. 148, pp. 292.
- 701 Darby, D.A., Polyak, L., Bauch, H.A., 2006. Past glacial and interglacial conditions in the Arctic Ocean
702 and marginal seas - a review. *Prog. Oceanogr.* 71, 129-144.
- 703 Dowdeswell, J.A., Hogan, K.A., Evans, J., Noormets, R., Ó Cofaigh, C., Ottesen, D., 2010. Past ice-
704 sheet flow east of Svalbard inferred from streamlined subglacial landforms. *Geology* 38, 163-
705 166.
- 706 Dowdeswell, J.A., Ottesen, D., Bellec, V.K., 2020. The changing extent of marine-terminating glaciers
707 and ice caps in northeastern Svalbard since the 'Little Ice Age' from marine-geophysical records.
708 *The Holocene* 30, 389-401.
- 709 Ebbesen, H., Hald, M., Eplet, T.H., 2007. Lateglacial and early Holocene climatic oscillations on the
710 western Svalbard margin, *European Arctic. Quat. Sci. Rev.* 26, 1999-2011.
- 711 Elverhøi, A., Andersen, E.S., Dokken, T., Hebbeln, D., Spielhagen, R., Svendsen, J.I., Sørflaten, M.,
712 Rørnes, A., Hald, M., Forsberg, C.F., 1995. The growth and decay of the Late Weichselian ice
713 sheet in western Svalbard and adjacent areas based on provenance studies of marine sediments.
714 *Quat. Res.* 44, 303-316.
- 715 Farnsworth, W.R., Allaart, L., Ingólfsson, Ó., Alexanderson, H., Forwick, M., Noormets, R., Retelle,
716 M., Schomacker, A., 2020. Holocene glacial history of Svalbard: Status, perspectives and
717 challenges. *Earth-Sci. Rev.* 208, 103249.
- 718 Fjeldskaar, W., Bondevik, S., Amantov, A., 2018. Glaciers on Svalbard survived the Holocene thermal
719 optimum. *Quat. Sci. Rev.* 199, 18-29.
- 720 Flink, A.E., Noormets, R., Fransner, O., Hogan, K.A., ÓRegan, M., Jakobsson, M., 2017. Past ice flow
721 in Wahlenbergfjorden and its implications for late Quaternary ice sheet dynamics in northeastern
722 Svalbard. *Quat. Sci. Rev.* 163, 162-179.
- 723 Folk, R.L., Ward, W.C., 1957. Brazos River bar [Texas]; a study in the significance of grain size
724 parameters. *J. Sediment. Res.* 27, 3-26.
- 725 Forman, S., Lubinski, D., Ingólfsson, Ó., Zeeberg, J., Snyder, J., Siegert, M., Matishov, G., 2004. A

- 726 review of postglacial emergence on Svalbard, Franz Josef Land and Novaya Zemlya, northern
727 Eurasia. *Quat. Sci. Rev.* 23, 1391-1434.
- 728 Fortey, R.A., Bruton, D.L., 1973. Cambrian-Ordovician rocks adjacent to Hinlopenstretet, north Ny
729 Friesland, Spitsbergen. *Geol. S. Am. Bull.* 84, 2227-2242.
- 730 Forwick, M., Vorren, T.O., 2007. Holocene mass-transport activity and climate in outer Isfjorden,
731 Spitsbergen: marine and subsurface evidence. *The Holocene* 17, 707-716.
- 732 Forwick, M., Vorren, T.O., 2009. Late Weichselian and Holocene sedimentary environments and ice
733 rafting in Isfjorden, Spitsbergen. *Palaeogeogr. Palaeoclimatol. Palaeoecol.* 280, 258-274.
- 734 Forwick, M., Vorren, T.O., Hald, M., Korsun, S., Roh, Y., Vogt, C., Yoo, K.-C., 2010. Spatial and
735 temporal influence of glaciers and rivers on the sedimentary environment in Sassenfjorden and
736 Tempelfjorden, Spitsbergen. *Geol. Soc. Lond., Spec. Publ.* 344, 163-193.
- 737 Goldstein, S.L., Hemming, S.R., 2003. Long-lived isotopic tracers in oceanography, paleoceanography,
738 and ice-sheet dynamics, in: Elderfield, H. (Ed.), *Treatise on Geochemistry*. Elsevier, Oxford, pp.
739 453-489.
- 740 Grousset, F., Biscaye, P., Zindler, A., Prospero, J., Chester, R., 1988. Neodymium isotopes as tracers in
741 marine sediments and aerosols: North Atlantic. *Earth Planet. Sci. Lett.* 87, 367-378.
- 742 Hald, M., Dahlgren, T., Olsen, T.-E., Lebesbye, E., 2001. Late Holocene palaeoceanography in Van
743 Mijenfjorden, Svalbard. *Polar Res.* 20, 23-35.
- 744 Hald, M., Ebbesen, H., Forwick, M., Godtlielsen, F., Khomenko, L., Korsun, S., Olsen, L.R., Vorren,
745 T.O., 2004. Holocene paleoceanography and glacial history of the West Spitsbergen area, Euro-
746 Arctic margin. *Quat. Sci. Rev.* 23, 2075-2088.
- 747 Haley, B.A., Polyak, L., 2013. Pre-modern Arctic Ocean circulation from surface sediment neodymium
748 isotopes. *Geophys. Res. Lett.* 40, 893-897.
- 749 Hindshaw, R.S., Aciego, S.M., Piotrowski, A.M., Tipper, E.T., 2018. Decoupling of dissolved and
750 bedrock neodymium isotopes during sedimentary cycling. *Geochem. Perspect. Lett.* 8, 43-46.
- 751 Hjelle, A., 1993. *Geology of Svalbard*. Norsk Polarinsti. Oslo, pp. 163.
- 752 Hogan, K.A., Dowdeswell, J.A., Hillenbrand, C.-D., Ehrmann, W., Noormets, R., Wacker, L., 2017.

- 753 Subglacial sediment pathways and deglacial chronology of the northern Barents Sea Ice Sheet.
754 *Boreas* 46, 750-771.
- 755 Horikawa, K., Martin, E.E., Basak, C., Onodera, J., Seki, O., Sakamoto, T., Ikehara, M., Sakai, S.,
756 Kawamura, K., 2015. Pliocene cooling enhanced by flow of low-salinity Bering Sea water to
757 the Arctic Ocean. *Nat. Commun.* 6, doi.org/10.1038/ncomms8587.
- 758 Hormes, A., Akçar, N., Kubik, P.W., 2011. Cosmogenic radionuclide dating indicates ice-sheet
759 configuration during MIS 2 on Nordaustlandet, Svalbard. *Boreas* 40, 636-649.
- 760 Hughes, A.L., Gyllencreutz, R., Lohne, Ø.S., Mangerud, J., Svendsen, J.I., 2016. The last Eurasian ice
761 sheets—a chronological database and time-slice reconstruction, DATED-1. *Boreas* 45, 1-45.
- 762 Jacobsen, S.B., Wasserburg, G.J., 1980. Sm-Nd isotopic evolution of chondrites. *Earth Planet. Sci. Lett.*
763 50, 139-155.
- 764 Jakobsson, M., Andreassen, K., Bjarnadóttir, L.R., Dove, D., Dowdeswell, J.A., England, J.H., Funder,
765 S., Hogan, K., Ingólfsson, Ó., Jennings, A., Krog Larsen, N., Kirchner, N., Landvik, J.Y., Mayer,
766 L., Mikkelsen, N., Möller, P., Niessen, F., Nilsson, J., O'Regan, M., Polyak, L., Nørgaard-
767 Pedersen, N., Stein, R., 2014. Arctic Ocean glacial history. *Quat. Sci. Rev.* 92, 40-67.
- 768 Jang, K., Bayon, G., Han, Y., Joo, Y.J., Kim, J.-H., Ryu, J.-S., Woo, J., Forwick, M., Szczuciński, W.,
769 Kim, J.-H., Nam, S.-I., 2020. Neodymium isotope constraints on chemical weathering and past
770 glacial activity in Svalbard. *Earth Planet. Sci. Lett.* 542, 116319.
- 771 Jang, K., Han, Y., Huh, Y., Nam, S.-I., Stein, R., Mackensen, A., Matthiessen, J., 2013. Glacial
772 freshwater discharge events recorded by authigenic neodymium isotopes in sediments from the
773 Mendeleev Ridge, western Arctic Ocean. *Earth Planet. Sci. Lett.* 369-370, 148-157.
- 774 Jang, K., Huh, Y., Han, Y., 2017. Authigenic Nd isotope record of North Pacific Intermediate Water
775 formation and boundary exchange on the Bering Slope. *Quat. Sci. Rev.* 156, 150-163.
- 776 Jernas, P., Klitgaard Kristensen, D., Husum, K., Wilson, L., Koç, N., 2013. Palaeoenvironmental
777 changes of the last two millennia on the western and northern Svalbard shelf. *Boreas* 42, 236-
778 255.
- 779 Jessen, S.P., Rasmussen, T.L., Nielsen, T., Solheim, A., 2010. A new Late Weichselian and Holocene

- 780 marine chronology for the western Svalbard slope 30,000–0 cal years BP. *Quat. Sci. Rev.* 29,
781 1301-1312.
- 782 Johansson, Å., Gee, D., Björklund, L., Witt-Nilsson, P., 1995. Isotope studies of granitoids from the
783 Bangenhuk formation, Ny Friesland Caledonides, Svalbard. *Geol. Mag.* 132, 303-320.
- 784 Johansson, Å., Gee, D.G., 1999. The late Palaeoproterozoic Eskolabreen granitoids of southern Ny
785 Friesland, Svalbard Caledonides-geochemistry, age, and origin. *GFF* 121, 113-126.
- 786 Johansson, Å., Larionov, A.N., Tebenkov, A.M., Gee, D.G., Whitehouse, M.J., Vestin, J., 2000.
787 Grenvillian magmatism of western and central Nordaustlandet, northeastern Svalbard. *Earth Env.*
788 *Sci. T. R. So.* 90, 221-254.
- 789 Johansson, Å., Larionov, A.N., Tebenkov, A.M., Ohta, Y., Gee, D.G., 2002. Caledonian granites of
790 western and central Nordaustlandet, northeast Svalbard. *GFF* 124, 135-148.
- 791 Jonkers, L., Zahn, R., Thomas, A., Henderson, G., Abouchami, W., François, R., Masque, P., Hall, I.R.,
792 Bickert, T., 2015. Deep circulation changes in the central South Atlantic during the past 145 kyrs
793 reflected in a combined $^{231}\text{Pa}/^{230}\text{Th}$, neodymium isotope and benthic $\delta^{13}\text{C}$ record. *Earth Planet.*
794 *Sci. Lett.* 419, 14-21.
- 795 Kempf, P., Forwick, M., Laberg, J.S., Vorren, T.O., 2013. Late Weichselian and Holocene sedimentary
796 palaeoenvironment and glacial activity in the high-arctic van Keulenfjorden, Spitsbergen. *The*
797 *Holocene* 23, 1607-1618.
- 798 Kleiber, H., Knies, J., Niessen, F., 2000. The Late Weichselian glaciation of the Franz Victoria Trough,
799 northern Barents Sea: ice sheet extent and timing. *Mar. Geol.* 168, 25-44.
- 800 Knies, J., Kleiber, H.-P., Matthiessen, J., Müller, C., Nowaczyk, N., 2001. Marine ice-rafted debris
801 records constrain maximum extent of Saalian and Weichselian ice-sheets along the northern
802 Eurasian margin. *Global Planet. Change* 31, 45-64.
- 803 Knies, J., Martinez, P., 2009. Organic matter sedimentation in the western Barents Sea region:
804 Terrestrial and marine contribution based on isotopic composition and organic nitrogen content.
805 *Norw. J. Geol.* 89, 79-89.
- 806 Koç, N., Klitgaard-Kristensen, D., Hasle, K., Forsberg, C.F., Solheim, A., 2002. Late glacial

- 807 palaeoceanography of Hinlopen Strait, northern Svalbard. *Polar Res.* 21, 307-314.
- 808 Kunzmann, M., Halverson, G.P., Scott, C., Minarik, W.G., Wing, B.A., 2015. Geochemistry of
809 Neoproterozoic black shales from Svalbard: Implications for oceanic redox conditions spanning
810 Cryogenian glaciations. *Chem. Geol.* 417, 383-393.
- 811 Landvik, J.Y., Bondebik, S., Elyerhoi, A., Fjeldskaar, W., Mangerud, J., Siegert, S., Salvigsen, O.,
812 Svendsen, J.-I., Vorren, T.O., 1998. The last glacial maximum of Svalbard and the Barents Sea
813 area: ice sheet extent and configuration. *Quat. Sci. Rev.* 17, 43-76.
- 814 Laukert, G., Frank, M., Bauch, D., Hathorne, E.C., Rabe, B., von Appen, W.-J., Wegner, C., Zieringer,
815 M., Kassens, H., 2017. Ocean circulation and freshwater pathways in the Arctic Mediterranean
816 based on a combined Nd isotope, REE and oxygen isotope section across Fram Strait. *Geochim.*
817 *Cosmochim. Acta* 202, 285-309.
- 818 Lauritzen, Ø., 1981. Investigations of Carboniferous and Permian sediments in Svalbard. *Norsk*
819 *Polarinsti. Skri.* 176, pp. 47.
- 820 Maccali, J., Hillaire-Marcel, C., Carignan, J., Reisberg, L.C., 2013. Geochemical signatures of
821 sediments documenting Arctic sea-ice and water mass export through Fram Strait since the Last
822 Glacial Maximum. *Quat. Sci. Rev.* 64, 136-151.
- 823 Mackiewicz, N.E., Powell, R.D., Carlson, P.R., Molnia, B.F., 1984. Interlaminated ice-proximal
824 glacial marine sediments in Muir Inlet, Alaska. *Mar. Geol.* 57, 113-147.
- 825 Mangerud, J., Bondevik, S., Gulliksen, S., Karin Hufthammer, A., Høisæter, T., 2006. Marine ¹⁴C
826 reservoir ages for 19th century whales and molluscs from the North Atlantic. *Quat. Sci. Rev.* 25,
827 3228-3245.
- 828 Martín-Moreno, R., Allende Álvarez, F., Hagen, J.O., 2017. 'Little Ice Age' glacier extent and
829 subsequent retreat in Svalbard archipelago. *The Holocene* 27, 1379-1390.
- 830 Menze, S., Ingvaldsen, R.B., Haugan, P., Fer, I., Sundfjord, A., Beszczynska-Moeller, A., Falk-Petersen,
831 S., 2019. Atlantic water pathways along the north-western Svalbard shelf mapped using vessel-
832 mounted current profilers. *J. Geophys. Res. Oceans* 124, 1699-1716.
- 833 Moore, D.M., Reynolds Jr, R.C., 1989. X-ray Diffraction and the Identification and Analysis of Clay

- 834 Minerals. Oxford University Press (OUP), pp. 179-201.
- 835 Nuth, C., Kohler, J., König, M., Deschwenden, A.v., Hagen, J.O.M., Käab, A., Moholdt, G., Pettersson,
836 R., 2013. Decadal changes from a multi-temporal glacier inventory of Svalbard. *The Cryosphere*
837 7, 1603-1621.
- 838 Ó Cofaigh, C., Dowdeswell, J.A., 2001. Laminated sediments in glacial marine environments: diagnostic
839 criteria for their interpretation. *Quat. Sci. Rev.* 20, 1411-1436.
- 840 Ottesen, D., Dowdeswell, J.A., Landvik, J.Y., Mienert, J., 2007. Dynamics of the Late Weichselian ice
841 sheet on Svalbard inferred from high-resolution sea-floor morphology. *Boreas* 36, 286-306.
- 842 Patton, H., Hubbard, A., Andreassen, K., Auriac, A., Whitehouse, P.L., Stroeven, A.P., Shackleton, C.,
843 Winsborrow, M., Heyman, J., Hall, A.M., 2017. Deglaciation of the Eurasian ice sheet complex.
844 *Quat. Sci. Rev.* 169, 148-172.
- 845 Patton, H., Hubbard, A., Andreassen, K., Winsborrow, M., Stroeven, A.P., 2016. The build-up,
846 configuration, and dynamical sensitivity of the Eurasian ice-sheet complex to Late Weichselian
847 climatic and oceanic forcing. *Quat. Sci. Rev.* 153, 97-121.
- 848 Pereira, P.S., Flierdt, T.v.d., Hemming, S.R., Frederichs, T., Hammond, S.J., Brachfeld, S., Doherty, C.,
849 Kuhn, G., Smith, J.A., Klages, J.P., Hillenbrand, C.-D., 2020. The geochemical and
850 mineralogical fingerprint of West Antarctica's weak underbelly: Pine Island and Thwaites
851 glaciers. *Chem. Geol.* 550, 119649.
- 852 Petschick, R., Kuhn, G., Gingele, F., 1996. Clay mineral distribution in surface sediments of the South
853 Atlantic: sources, transport, and relation to oceanography. *Mar. Geol.* 130, 203-229.
- 854 Pfirman, S., Colony, R., Nürnberg, D., Eicken, H., Rigor, I., 1997. Reconstructing the origin and
855 trajectory of drifting Arctic sea ice. *J. Geophys. Res. Oceans* 102, 12575-12586.
- 856 Pin, C., Zalduegui, J.S., 1997. Sequential separation of light rare-earth elements, thorium and uranium
857 by miniaturized extraction chromatography: Application to isotopic analyses of silicate rocks.
858 *Anal. Chim. Acta* 339, 79-89.
- 859 Piotrowski, A.M., Goldstein, S.L., Hemming, S.R., Fairbanks, R.G., 2005. Temporal relationships of
860 carbon cycling and ocean circulation at glacial boundaries. *Science* 307, 1933-1938.

- 861 Raczek, I., Jochum, K.P., Hofmann, A.W., 2003. Neodymium and strontium isotope data for USGS
862 reference materials BCR-1, BCR-2, BHVO-1, BHVO-2, AGV-1, AGV-2, GSP-1, GSP-2 and
863 eight MPI-DING reference glasses. *Geostandard. Newslett.* 27, 173-179.
- 864 Rahaman, W., Smik, L., Köseoğlu, D., N, L., Tarique, M., Thamban, M., Haywood, A., Belt, S.T., Knies,
865 J., 2020. Reduced Arctic sea ice extent during the mid-Pliocene Warm Period concurrent with
866 increased Atlantic-climate regime. *Earth Planet. Sci. Lett.* 550, 116535.
- 867 Rasmussen, T.L., Thomsen, E., 2013. Pink marine sediments reveal rapid ice melt and Arctic meltwater
868 discharge during Dansgaard–Oeschger warmings. *Nat. Commun.* 4, 1-8.
- 869 Rasmussen, T.L., Thomsen, E., 2014. Brine formation in relation to climate changes and ice retreat
870 during the last 15,000 years in Storfjorden, Svalbard, 76–78 N. *Paleoceanography* 29, 911-929.
- 871 Rasmussen, T.L., Thomsen, E., Ślubowska, M.A., Jessen, S., Solheim, A., Koç, N., 2007.
872 Paleooceanographic evolution of the SW Svalbard margin (76°N) since 20,000 ¹⁴C yr BP. *Quat.*
873 *Res.* 67, 100-114.
- 874 Revel, M., Sinko, J.A., Grousset, F.E., Biscaye, P.E., 1996. Sr and Nd isotopes as tracers of North
875 Atlantic lithic particles: Paleoclimatic implications. *Paleoceanography* 11, 95-113.
- 876 Rutberg, R.L., Hemming, S.R., Goldstein, S.L., 2000. Reduced North Atlantic Deep Water flux to the
877 glacial Southern Ocean inferred from neodymium isotope ratios. *Nature* 405, 935-938.
- 878 Røthe, T.O., Bakke, J., Vasskog, K., Gjerde, M., D'Andrea, W.J., Bradley, R.S., 2015. Arctic Holocene
879 glacier fluctuations reconstructed from lake sediments at Mitrahelvøya, Spitsbergen. *Quat. Sci.*
880 *Rev.* 109, 111-125.
- 881 Silva, J.A., Bremner, J.M., 1966. Determination and isotope-ratio analysis of different forms of nitrogen
882 in soils: 5. Fixed Ammonium. *Soil Sci. Soc. Am. J.* 30, 587-594.
- 883 Ślubowska-Woldengen, M., Rasmussen, T.L., Koç, N., Klitgaard-Kristensen, D., Nilsen, F., Solheim,
884 A., 2007. Advection of Atlantic Water to the western and northern Svalbard shelf since 17,500
885 cal yr BP. *Quat. Sci. Rev.* 26, 463-478.
- 886 Ślubowska, M.A., Koç, N., Rasmussen, T.L., Klitgaard-Kristensen, D., 2005. Changes in the flow of
887 Atlantic water into the Arctic Ocean since the last deglaciation: evidence from the northern

- 888 Svalbard continental margin, 80°N. *Paleoceanography* 20, doi.org/10.1029/2005PA001141.
- 889 Stein, R., 2019. The late Mesozoic-Cenozoic Arctic Ocean climate and sea ice history: A challenge for
890 past and future scientific ocean drilling. *Paleoceanogr. Paleoclimatol.* 34, 1851-1894.
- 891 Sufke, F., Gutjahr, M., Gilli, A., Anselmetti, F.S., Glur, L., Eisenhauer, A., 2019. Early stage weathering
892 systematics of Pb and Nd isotopes derived from a high-Alpine Holocene lake sediment record.
893 *Chem. Geol.* 507, 42-53.
- 894 Stuiver, M., Reimer, P.J., 1993. Extended ¹⁴C data base and revised CALIB 3.0 ¹⁴C age calibration
895 program. *Radiocarbon* 35, 215-230.
- 896 Svendsen, J.I., Alexanderson, H., Astakhov, V.I., Demidov, I., Dowdeswell, J.A., Funder, S., Gataullin,
897 V., Henriksen, M., Hjort, C., Houmark-Nielsen, M., Hubberten, H.W., Ingólfsson, Ó., Jakobsson,
898 M., Kjær, K.H., Larsen, E., Lokrantz, H., Lunkka, J.P., Lyså, A., Mangerud, J., Matiouchkov, A.,
899 Murray, A., Möller, P., Niessen, F., Nikolskaya, O., Polyak, L., Saarnisto, M., Siegert, C., Siegert,
900 M.J., Spielhagen, R.F., Stein, R., 2004. Late Quaternary ice sheet history of northern Eurasia.
901 *Quat. Sci. Rev.* 23, 1229-1271.
- 902 Svendsen, J.I., Elverhøi, A., Mangerud, J., 1996. The retreat of the Barents Sea Ice Sheet on the western
903 Svalbard margin. *Boreas* 25, 244-256.
- 904 Svendsen, J.I., Mangerud, J., 1997. Holocene glacial and climatic variations on Spitsbergen, Svalbard.
905 *The Holocene* 7, 45-57.
- 906 Svendsen, J.I., Mangerud, J., Elverhøi, A., Solheim, A., Schüttenhelm, R.T., 1992. The Late Weichselian
907 glacial maximum on western Spitsbergen inferred from offshore sediment cores. *Mar. Geol.* 104,
908 1-17.
- 909 Tanaka, T., Togashi, S., Kamioka, H., Amakawa, H., Kagami, H., Hamamoto, T., Yuhara, M., Orihashi,
910 Y., Yoneda, S., Shimizu, H., Kunimaru, T., Takahashi, K., Yanagi, T., Nakano, T., Fujimaki, H.,
911 Shinjo, R., Asahara, Y., Tanimizu, M., Dragusanu, C., 2000. JNdi-1: a neodymium isotopic
912 reference in consistency with LaJolla neodymium. *Chem. Geol.* 168, 279-281.
- 913 Tarasov, L., Peltier, W., 2005. Arctic freshwater forcing of the Younger Dryas cold reversal. *Nature* 435,
914 662-665.

- 915 Teschner, C., Frank, M., Haley, B.A., Knies, J., 2016. Plio-Pleistocene evolution of water mass
916 exchange and erosional input at the Atlantic-Arctic gateway. *Paleoceanography* 31, 582-599.
- 917 Tian, S.Y., Yasuhara, M., Hong, Y., Huang, H.-H.M., Iwatani, H., Chiu, W.-T.R., Mamo, B., Okahashi,
918 H., Rasmussen, T.L., 2020. Deglacial–Holocene Svalbard paleoceanography and evidence of
919 meltwater pulse 1B. *Quat. Sci. Rev.* 233, 106237.
- 920 Tütken, T., Eisenhauer, A., Wiegand, B., Hansen, B.T., 2002. Glacial–interglacial cycles in Sr and Nd
921 isotopic composition of Arctic marine sediments triggered by the Svalbard/Barents Sea ice sheet.
922 *Mar. Geol.* 182, 351-372.
- 923 van der Bilt, W.G.M., Bakke, J., Vasskog, K., D'Andrea, W.J., Bradley, R.S., Ólafsdóttir, S., 2015.
924 Reconstruction of glacier variability from lake sediments reveals dynamic Holocene climate in
925 Svalbard. *Quat. Sci. Rev.* 126, 201-218.
- 926 Vogt, C., Lauterjung, J.r., Fischer, R.X., 2002. Investigation of the clay fraction (< 2 µm) of the clay
927 minerals society reference clays. *Clay. Clay Miner.* 50, 388-400.
- 928 Vorren, T.O., Plassen, L., 2002. Deglaciation and palaeoclimate of the Andfjord-Vågsfjord area, North
929 Norway. *Boreas* 31, 97-125.
- 930 Wadham, J.L., Hawkings, J.R., Tarasov, L., Gregoire, L.J., Spencer, R.G.M., Gutjahr, M., Ridgwell, A.,
931 Kohfeld, K.E., 2019. Ice sheets matter for the global carbon cycle. *Nat. Commun.* 10, 3567.
- 932 Werner, K., Frank, M., Teschner, C., Müller, J., Spielhagen, R.F., 2014. Neoglacial change in deep water
933 exchange and increase of sea-ice transport through eastern Fram Strait: evidence from
934 radiogenic isotopes. *Quat. Sci. Rev.* 92, 190-207.
- 935 Winkelmann, D., Knies, J., 2005. Recent distribution and accumulation of organic carbon on the
936 continental margin west off Spitsbergen. *Geochem. Geophys. Geosyst.* 6.
- 937
- 938